

Chapter 1

Manganese mineralogy and diagenesis in the sedimentary rock record

Jena E. Johnson^{1*}, Samuel M. Webb², Chi Ma¹, Woodward W. Fischer¹

¹Division of Geological and Planetary Sciences, California Institute of Technology,
Pasadena, CA 91125

²Stanford Synchrotron Radiation Lightsource, Stanford University, Menlo Park,
CA 94025

ABSTRACT

Oxidation of manganese(II) to manganese (III,IV) demands oxidants with very high redox potentials; consequently, manganese oxides are both excellent proxies for molecular oxygen and highly favorable electron acceptors when oxygen is absent. The first of these features results in manganese-enriched sedimentary rocks (manganese deposits, commonly Mn ore deposits), which generally correspond to the availability of molecular oxygen in Earth surface environments. And yet because manganese reduction is energetically favorable by a variety of chemical species, these ancient manganese deposits are often significantly more reduced than modern environmental manganese-rich sediments. We document the impacts of manganese reduction and the mineral phases that form stable manganese deposits from seven sedimentary examples spanning from the modern surface environments to rocks over 2 billion years old. Integrating redox and coordination information from

synchrotron X-ray absorption spectroscopy and X-ray microprobe imaging with scanning electron microscopy and energy and wavelength-dispersive spectroscopy, we find that unlike the Mn(IV)-dominated modern manganese deposits, three manganese minerals dominate these representative ancient deposits: kutnohorite ($\text{Mn}_{0.5}\text{Ca}_{0.5}\text{CO}_3$), rhodochrosite (MnCO_3), and braunite ($\text{Mn(III)}_6\text{Mn(II)}\text{O}_8\text{SiO}_4$). Pairing these mineral and textural observations with previous studies of manganese geochemistry, we develop a paragenetic model of post-depositional manganese mineralization with kutnohorite as the earliest diagenetic mineral phase and rhodochrosite and braunite forming secondarily.

1. INTRODUCTION

Manganese oxides are critical environmental reactants as powerful oxidants, scavengers of important trace elements and reactive oxygen species, and as electron acceptors for anaerobic respiration (C. R. Myers and Nealson, 1988; Tebo et al., 2005). Manganese is the third most abundant transition metal in Earth's crust and has the largest number of oxidation states of 3d row elements (Armstrong, 2008), and so consequently the manganese cycle involves multiple redox conversions.

Mn is present exclusively in divalent forms in a wide range of igneous minerals where it substitutes for iron (Post, 1999). It averages at 980 ppm or about 0.1% in ultrabasic, basaltic, granitic, and syenitic igneous rocks (Turekian and Wedepohl, 1961). However, in siliceous pegmatites, manganese can be more concentrated in garnets and phosphate

minerals, in addition to more obscure minerals like zirconosilicates, titanium silicates, and niobium and tantalum ore minerals (Iddings, 2009). Yet in bulk, pegmatites are still low in Mn, reaching up to approximately 0.23% Mn (Norton, 1970; Stilling, 1998; Akintola et al., 2012). Thus silicate weathering provides a substantial source of Mn^{2+} to surface and ground waters (Gross, 1965; Post, 1999). Mn^{2+} is also sourced from seafloor hydrothermal vents, at high but variable concentrations ranging from hundreds to thousands of micromoles per kilogram (Von Damm, 1990).

Manganese(II) is highly soluble, even more so than iron (Gross, 1965; Post, 1999). Strongly evaporative basins such as the Red Sea and Mediterranean Sea show no enrichment of manganese, but anoxic basins like the Black Sea can become enriched in soluble manganese(II) (Nicholson, 1997). To concentrate Mn into significant sedimentary deposits, manganese needs to be oxidized to Mn^{3+} or Mn^{4+} as these ions form insoluble oxyhydroxide minerals that are deposited in sediments (Calvert and Pedersen, 1996; Armstrong, 2008). Like iron, manganese is insoluble in its oxidized form, but unlike iron, manganese does not readily form sulfides (Van Cappellen et al., 1998; Maynard, 2010). Thus, the presence of significant manganese deposition in the sedimentary record should reflect the history of manganese oxidation.

However, there are a couple exceptions to this general pattern of manganese enrichment in the sediments signifying manganese oxidation. When there are high levels of soluble Mn^{2+} , this divalent ion can substitute for Ca^{2+} in carbonates and precipitate as Mn-

enriched carbonates. These carbonates are the main sink for Mn^{2+} : while other cations such as Na^+ are removed from seawater by pore water burial and reverse weathering reactions (Berner and Berner, 2012), measurements of pore water today indicate that carbonate precipitation and dissolution seem to primarily control dissolved manganese(II) concentrations (Wallmann et al., 2008). Mn levels in carbonates are often used as a characteristic marker for secondary alteration (Brand and Veizer, 1980) since pore-water fluids are often enriched in manganese: this is due to sedimentary pore waters becoming enriched in Mn^{2+} due to the reduction and dissolution of Mn(IV) oxides (Calvert and Pedersen, 1996; Van Cappellen et al., 1998) and the elevated Mn concentrations in hydrothermal fluids (Von Damm, 1990). Despite Mn usually signifying alteration, primary well-preserved carbonates from the Archean Eon (4 Ga to 2.5 Ga) have elevated Mn levels—up to 1% Mn rather than typical Phanerozoic carbonates of 10-50 ppm in well-preserved carbonates (Veizer, 1978; Brand and Veizer, 1980; Holland, 1984; Beukes, 1987; Komiya et al., 2008; Fischer and Knoll, 2009). These anomalous Mn-enriched carbonate platforms probably occur because the oceans during this time were anoxic and able to concentrate soluble Mn^{2+} to relatively high levels (estimated at 3 to 7 micromolar, (Holland, 1984)). Karst weathering, the near-surface dissolution of carbonates from interaction with meteoritic waters, of Mn-bearing carbonates after the rise of oxygen can lead to supergene concentration of Mn as the carbonate is dissolved and Mn^{2+} is oxidized; this process can produce small but economically meaningful Mn ores such as the Postmasburg and Woodie Woodie Mn deposits (Gutzmer, 1996; Jones et al., 2013).

The high Mn levels in Archean seawater are directly related to the lack of Mn oxidation before the rise of oxygen, approximately 2.3 billion years ago. There is a very limited set of processes and oxidants able to oxidize manganese due to its high redox potential (Tebo et al., 2004). Low levels of manganese oxidation are possible, in principle, from reactions with UV light, but this is suppressed in the presence of Fe^{2+} or other reductants (Anbar and Holland, 1992). Manganese is oxidized phototrophically during the biosynthesis of the water-oxidizing complex of Photosystem II in Cyanobacteria, plants, and algae (Tamura and Chéniaie, 1987; Büchel et al., 1999), but this is not thought to produce environmentally-significant manganese oxides (Madison et al., 2013) and no solely manganese-oxidizing photosystem has been documented in modern phototrophs (Johnson et al., 2013). With a notable exception (Johnson et al., 2013), Mn(II) is only oxidized at meaningful rates by molecular oxygen or O_2 -derived species like superoxide (Calvert and Pedersen, 1996; Post, 1999; Tebo et al., 2004; Morgan, 2005; Dick et al., 2009; Hansel et al., 2012), so the presence of manganese(III,IV) oxides in sedimentary rocks can indicate that free oxygen was once present in the environment.

Due to the unique high-potential redox chemistry of Mn, the geologic record of manganese deposits should reflect ancient oxygen availability and the paleo-environmental chemistry (Maynard, 2010). In Fig. 1, we present an updated compilation of Mn deposits through geologic time, and also plot size estimates of each terrestrial deposit (Fig. 1, Table 1). The lack of significant Archean Mn deposits is striking, as is the

massive Hotazel deposit at around 2.22 billion years ago (Ga). Several previous compilations have included small Archean manganese deposits (Roy, 2006; Maynard, 2010), but these appear to be derived from later weathering of Archean carbonate strata (which contain elevated Mn(II)), and thus we do not include them as the timing of the weathering is unknown (Roy, 2006). Since oxygen was introduced into the atmosphere and oceans around 2.3 billion years ago (Ga) (commonly known as the ‘Great Oxidation Event’, or rise of oxygen) (Bekker et al., 2004; Hoffman, 2013), it is interesting that the world’s largest terrestrial manganese deposit—estimated to be 13,500 million metric tons (Taljaart, 1982)—was deposited soon after this dramatic environmental change occurred (Kirschvink et al., 2000). Manganese deposition appears to be associated with the presence of environmental oxygen, since manganese deposits post-2.3 Ga are common (Fig.1). Thus, Mn deposits provide insight into redox processes operating in surface environments on Earth.

To understand the genesis of Mn deposits in greater mechanistic detail, we chose to carefully investigate representative samples from seven globally-distributed manganese deposits spanning from the modern to 2.41 billion years ago. We coupled petrography and sedimentary geology using optical and electron microscopy with microscale X-ray absorption spectroscopy (XAS) imaging to better understand the manganese minerals present and the processes that produced them. From previous surveys of geologic manganese deposits, it is clear that there are significant variations in which manganese minerals are present in ancient manganese deposits (Okita et al., 1988; Roy, 2006;

Maynard, 2010); notably, the redox state of manganese varies in these minerals from Mn(II) to Mn(III) to Mn(IV). Maynard (2010) summarized the major minerals in manganese deposits as being braunite, a mixed valence Mn(III/II) oxide, and rhodochrosite, a Mn carbonate salt. He found that rhodochrosite dominated in sedimentary environments, braunite in volcanic deposits, and other Mn oxides in karstic and supergene environments (Maynard, 2010). Within sedimentary deposits, he proposed that rhodochrosite was a primary or early diagenetic (secondary) Mn mineral and that other Mn silicates and oxides (like braunite) arose during late diagenesis, metamorphism, or supergene alteration, but the only evidence for this hypothesis arose from ^{13}C -depleted rhodochrosite in the major Mn deposits (Maynard, 2010). We tested this theory of manganese mineral paragenesis using classic sedimentological and petrographic observations at the scale of textures and mineral grains. We applied our microscale analyses to a range of sedimentary deposits to identify the sequence of mineralogical changes that occur to manganese deposits from deposition through early diagenesis, and metamorphism to near-surface oxidative weathering. These observations of manganese mineralization enable us to infer the likely primary precipitates that concentrated Mn in ancient sediments and the post-depositional processes that subsequently altered the manganese mineralogy and stabilized it in the rock record.

We begin by introducing the relevant environmental chemistry and biological influences on the modern manganese cycle, describe our observations of manganese deposits across

geologic time and paleo-environment, and then discuss how to connect biogeochemical processes to the rock record of manganese deposits.

1.1 Modern Manganese oxidation

Several natural processes that oxidize Mn(II) to Mn oxides are currently known: all are either caused by O₂ or species derived from O₂ (like reactive oxygen species) or related to the photosynthetic production of O₂. Prior to water-splitting and the production of molecular oxygen, Mn(II) is oxidized to Mn(III) and Mn(IV) in the high-valent tetra-manganese water-oxidizing complex of photosystem II (Tamura and Chéniaie, 1987; Büchel et al., 1999). To date, this is the only phototrophic mechanism known to oxidize Mn(II), with all currently known anoxygenic photosystems unable to generate the necessary high redox potential necessary for Mn oxidation. Abiotic photochemical oxidation of Mn(II) is slow and further hampered by the presence of other reductants such as Fe(II) (Anbar and Holland, 1992). Consequently, the presence of manganese oxides is generally associated with oxygen availability.

Today effectively all aquatic Mn-oxidation is controlled by biology (Tebo et al., 2004; Geszvain et al., 2012). Manganese oxidation by aerobic microorganisms occurs in diverse groups of bacteria (Firmicutes, Actinobacteria, Alphaproteobacteria, Gammaproteobacteria, and Betaproteobacteria) as well as in several types of fungi (in the Basidiomycota and Ascomycota phyla) (Hansel et al., 2012; Geszvain et al., 2012). The adaptive function of this physiology remains unclear, and none of these organisms are

known to conserve energy through this process. The pervasive distribution of Mn-oxidizing capabilities throughout such a diversity of organisms suggests that there may be multiple advantages to performing this reaction. A variety of potential functions for Mn oxidation has been proposed, including protection from UV light, predation, viruses, toxins, and reactive oxygen species, or the breakdown of refractory organic polymers into more readily usable compounds, the storage of an electron acceptor for future anaerobic respiration, or the scavenging of trace metals for micronutrient requirements (Tebo et al., 2004).

The mechanisms of microbial manganese oxidation are somewhat better understood than the biological purposes of the reaction. Some bacteria, like *Bacillus* species, use outer membrane multicopper oxidase enzymes to oxidize Mn(II) to Mn(III) and then to Mn(IV) in two sequential enzymatic oxidation steps (Samuel M. Webb et al., 2005), where the final released product is a Mn(IV)-dominated oxide like birnessite (a manganese(IV) oxide with variable amounts of Mn(III) due to substitution by Na, K, and Ca) (Bargar et al., 2000; John R Bargar et al., 2005; S. M. Webb et al., 2005; Butterfield et al., 2013). Other bacteria, like the alphaproteobacteria *Aurantimonas manganoxydans* and an *Erythrobacter* strain, appear to use an animal heme peroxidase enzyme to oxidize Mn(II) to Mn(III), which may represent an independent Mn-oxidizing mechanism in bacteria using H₂O₂ or which may work in concert with multicopper oxidases (Anderson et al., 2009). Certain fungi, like the Basidiomycete fungi, also use manganese peroxidase to oxidize Mn(II) to Mn(III) via H₂O₂ (Wariishi et al., 1992). In this better-studied fungal

system, the Mn(III) produced by these peroxidases is used to form reactive complexes with organic molecules, which then can be utilized to degrade lignin and become catalytically re-reduced to Mn(II) (Hammel et al., 1989; Perez and Jeffries, 1992). If not properly ligated, the Mn(III) disproportionates to Mn(II) and Mn(IV) oxide phases (Perez and Jeffries, 1992) and the ultimate manganese product from fungal Mn oxidation appears to be birnessite-like Mn(IV) oxide phases (Santelli et al., 2011). Recently, manganese oxidation via superoxide production has been discovered in both bacteria and fungi (Learman et al., 2011; Hansel et al., 2012). This superoxide-stimulated oxidation appears to proceed through an Mn(III) intermediate, with some loss to Mn(III) ligands but eventually producing a final Mn(IV) oxide precipitate that is poorly crystalline, similar to other biologically produced Mn-oxides (Learman et al., 2011; Hansel et al., 2012). While it is difficult to tie environmental data to a specific molecular oxidation mechanism, rates of microbial manganese oxidation in the environment have been measured up to 50 nM per hr (Clement et al., 2009), yielding an oxidation rate constant of up to $\sim 10 \text{ hr}^{-1}$ (Morgan, 2005). These rates are much more rapid than abiotic oxidation mechanisms and indicate that microbial manganese oxidation is a key feature in the oxidation of Mn(II) in marine waters, and potentially in a wide variety of environments.

Mn(II) oxidation will also occur abiotically from reaction with environmental O_2 , but the oxidation is thermodynamically inhibited by the first electron transfer step (Diem and Stumm, 1984; Morgan, 2005; Luther, 2010). For homogenous oxidation (without any surface catalyst), Morgan (2005) estimated the oxidation rate constant to be 10^{-4} hr^{-1}

under modern atmospheric conditions, pH 8 and 7.5 μM Mn(II). This implies a Mn(II) half-life of 200 to 300 days, and measurements suggest similar rates in sterile seawater (von Langen et al., 1997; Morgan, 2005). Experimental results indicate that Mn(II) is first oxidized by O_2 to either the Mn(II,III) oxide hausmannite (Mn_3O_4) or the Mn(III) oxyhydroxide feitknechtite ($\beta\text{-MnOOH}$) (Hem and Lind, 1983). While these phases can be stable for months, eventually disproportionation reactions will yield the more stable phases and species of MnO_2 and Mn^{2+} , respectively (Hem and Lind, 1983; Murray et al., 1985). Metal oxide surfaces can hasten this abiotic oxidation reaction due to adsorption-oxidation processes, with an oxidation rate about an order of magnitude greater under modern O_2 levels (10^{-3} hr^{-1} , (Davies and Morgan, 1989; Morgan, 2005). Laboratory experiments have measured feitknechtite ($\beta\text{-MnOOH}$) as the primary precipitate from these surface-stimulated (or heterogeneous) Mn oxidation reactions (Junta and Hochella Jr., 1994). Junta and Hochella measured manganite (a more stable form of Mn(III) oxyhydroxide, $\gamma\text{-MnOOH}$) as a secondary product. These experiments also suggested that the modeled abiotic oxidation rates may be underestimating the amount of oxidation occurring, as micro-scale techniques revealed Mn oxide formation within minutes (Junta and Hochella Jr., 1994; Junta-Rosso and Hochella Jr., 1996). While these abiotic Mn(III) oxyhydroxides were quite stable, the authors hypothesized that the Mn(III) oxyhydroxides would disproportionate to form Mn^{2+} and pyrolusite ($\beta\text{-MnO}_2$) or birnessite.

Another way Mn(III) phases form is by redox reactions between Mn^{2+} and Mn(IV) oxides, known as comproportionation reactions. Bargar et al (2005) demonstrated that in abiotic experiments, Mn(IV) and aqueous Mn(II) reacted to form feitknechtite (β - MnOOH); this Mn(III) product was stable for days (John R. Bargar et al., 2005). Mandernack et al (1995) had calculated that feitknechtite-sodium birnessite equilibrium occurred at approximately 500 μM Mn(II), implying that birnessite will be stable at Mn(II) concentrations below 500 μM but for Mn(II) levels higher than 500 μM , feitknechtite will be stable. The comproportionation process to form the Mn(III) in feitknechtite involves electron transfer from adsorbed Mn^{2+} to Mn(IV) atoms in birnessite; feitknechtite was later replaced by manganite (MnOOH), a more stable Mn(III) oxyhydroxide (Elzinga, 2011).

Recent studies observed abundant Mn(III) in suboxic water and sediments, stabilized by organic complexes (Trouwborst et al., 2006; Madison et al., 2013). This Mn(III) was determined to be dominantly formed during Mn(II) oxidation by O_2 , but may also be produced during biotic and abiotic Mn(IV) reduction and by photosynthetic Mn(II) oxidation during oxygenic photosynthesis to a lesser extent (Madison et al., 2013). At low oxygen levels (3 to 25 μM), up to 90% of the Mn was in soluble Mn(III) complexes, likely stabilized by organic ligands (Madison et al., 2013). This Mn(III) can participate in redox reactions in the suboxic zone, but would be reduced to Mn(II) or oxidized to Mn(IV) if exposed to different redox conditions (Madison et al., 2013). As reactive intermediates, these Mn(III) complexes can participate in both reduction and oxidation

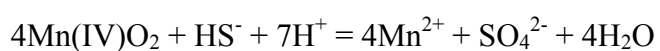
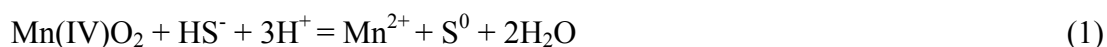
reactions and thus be a powerful addition to the redox cycling that occurs in suboxic zones (Madison et al., 2013).

Regardless of whether the oxidation mechanism is abiotic or biologically-mediated, the final products of manganese oxidation seem to be Mn(IV) oxides such as birnessite and pyrolusite. When observed in the environment, Mn(IV)-dominated, poorly crystalline, layered oxides are the ultimate product of Mn(II) oxidation in the Saanich Inlet, the Black Sea, desert varnish, lake sediments, and Pacific ocean sediments (Murray et al., 1985; Wehrli et al., 1995; McKeown and Post, 2001; Tebo et al., 2004).

1.2 Modern manganese reduction

From comparing the reduction-oxidation (redox) potentials of Mn and other redox-active ions and molecules, the thermodynamics of manganese oxide reduction is highly favorable when coupled to common environmental reductants. Furthermore, the kinetics of Mn(IV)-oxide reduction, unlike Mn(II) oxidation, are rapid (Stone and Morgan, 1984; Dollhopf et al., 2000). Manganese oxide reduction has been documented in many experiments, from more common species such as sulfide and ferrous iron (Burdige and Nealson, 1986; C.R. Myers and Nealson, 1988; Thamdrup et al., 1993) to less common As- and U-bearing compounds (Fredrickson et al., 2008; Ying et al., 2011). More complex aromatic organic molecules related to humic substances have also been shown to reduce manganese oxides (mainly Mn(III)), while simpler aromatic substrates like carboxylic acids were unreactive (Stone and Morgan, 1984). The electron donor in these

reactions is important: for example, in sulfide-coupled manganese(IV) reduction that produces both elemental sulfur (Burdige and Nealson, 1986) and/or sulfate (Aller and Rude, 1988; Thamdrup et al., 1993), protons are required and thus these reactions are a source of alkalinity:



The alkalinity that this reaction produces (4 to 7 units/ mole MnO_2) contrasts with another common mechanism to reduce manganese, coupling Mn(IV) reduction to iron oxidation:



When reduced by iron, manganese reduction actually produces protons and decreases alkalinity. More studies are needed to understand how prevalent these abiotic Mn(IV) reduction reactions are in nature.

Another mechanism of manganese oxide reduction occurs when dissimilatory metal-reducing microbes respire manganese oxides, depositing electrons on Mn(III,IV) oxides and generating Mn(II) while oxidizing organic carbon. Using a generic form for organic

carbon, this reaction produces alkalinity (2 units/ mole MnO₂), although not as much as sulfide-induced Mn reduction:



Using lactate or pyruvate (more complex and realistic organic substrates), the reaction produces roughly the same amount of alkalinity (2.2 units/ mole MnO₂; the alkalinity yield will only change substantially with more reduced C substrates). This type of anaerobic respiration was discovered in the 1980s in *Shewanella oneidensis* and *Geobacter* (Lovley and Phillips, 1988; C. R. Myers and Nealson, 1988) and has been widely documented in modern environments (e.g., Aller, 1990; Van Cappellen et al., 1998; Thamdrup et al., 2000). It can be difficult to diagnose what reductant or type of reduction, abiotic or biotic, results in the disappearance of Mn oxides and Mn²⁺ release (e.g., Canfield et al., 1993). However, the prevalence of Mn-reducing bacteria (for example, the well-studied metal-reducing *Shewanella* species have been found in marine, freshwater, soil, and sedimentary environments) suggests that a large portion of manganese reduction is microbially mediated.

Environmentally, evidence for manganese oxide reduction in soils and sediments is abundant (Aller, 1990; Canfield et al., 1993; Calvert and Pedersen, 1996; Van Cappellen et al., 1998; Thamdrup et al., 2000). When manganese oxides are deposited in marine sediments and subsequent manganese reduction (biotic or abiotic) occurs in sedimentary

pore waters, the Mn(II) concentrations increase dramatically—from the nanomolar Mn(II) concentrations in seawater to tens of micromolar in porewaters (Calvert and Pedersen, 1996). If there is sufficient dissolved inorganic carbon, especially if organic carbon is being respired using Mn(IV) oxides, Fe(III) oxides, or sulfate to produce additional CO₂, then Mn(II) and CO₃²⁻ can become supersaturated and manganese-bearing carbonates will precipitate (Calvert and Pedersen, 1996; Bergmann et al., 2013):



Because of the alkalinity produced (Reaction 3), Mn-carbonate precipitation is directly promoted by Mn oxide reduction without any need for other types of respiration.

Indeed, manganese carbonate precipitation from microbial manganese oxide reduction has been widely observed in laboratory experiments (Fischer et al., 2008; Ying et al., 2011; Lee et al., 2011). Ancient manganese carbonates have also been interpreted as products from Mn(IV) oxide reduction by heterotrophic organisms (e.g., Coleman et al., 1982; Okita et al., 1988; Matsumoto, 1992; Okita and Shanks, 1992; Johnson et al., 2013). A key line of evidence for this hypothesis is in the carbon isotopes of the manganese carbonates from these deposits: they are variably but strongly ¹³C-depleted, suggesting that their carbon is derived from mixtures of dissolved inorganic carbon from seawater and CO₂ originating from ¹³C-depleted sedimentary organic matter. Manganese oxides reduced stoichiometrically with organic compounds would produce ¹³C-depleted

CO₂, reduced Mn(II), and alkalinity (see Reaction 3), and these factors would promote the precipitation of Mn(II) carbonates and explain the unusual isotopic signatures of typical Mn-bearing carbonates in certain manganese deposits. Thus, not only does manganese reduction appear to be ubiquitous in modern environments, but this process appears to have ancient origins.

2. METHODS

Understanding the mineralogy, geochemistry, and petrogenesis of manganese-rich sedimentary rocks presents several challenges: the deposits are large but the materials are complex at fine scales, and thus require both microscale observations and basin-scale integration. The ideal way to determine redox state and mineral host at multiple scales is X-ray absorption spectroscopy coupled to light and electron microscopy techniques. Occasionally, more information is required, demanding the use of other methods.

One approach to assess the redox properties of manganese in a sample has focused on electron paramagnetic resonance (EPR) spectroscopy. EPR is an extremely sensitive technique to measure molecules with unpaired electrons (including Mn(II) and Mn(IV) species), and it has been useful for understanding the electronic structure and redox states of Mn in biochemical systems (see More et al., 1999; McEvoy and Brudvig, 2006). However, when this technique is applied to geological samples, results can become more complicated and nonunique. From observations of particularly narrow EPR line widths, it was suggested that EPR could be useful for distinguishing the biogenicity of the oxides

(Kim et al., 2011). Yet in concentrated geological samples, dipole-dipole interactions between closely packed Mn atoms affect the EPR signals (Pingitore Jr. et al., 1988). Thus, when Mn is concentrated in samples, it is difficult to distinguish Mn(II) minerals like rhodochrosite (MnCO_3) from Mn(III) or Mn(IV) minerals (Pingitore Jr. et al., 1988). Furthermore, EPR of samples is effectively a bulk measurement that requires sample homogenization and thus does not pair redox data to mineral textures.

A more ideal technique for manganese-rich rock samples is synchrotron-based X-ray absorption spectroscopy (XAS), a powerful method that measures the chemical properties of a specific element (or elements) within a sample. The absorption K-edge, or the ionization threshold of an element, is the energy required to remove an inner shell electron from an atom of that element. The absorption spectrum is sensitive to the local electronic and bonding environment of the absorbing element, and thus the absorption spectrum indicates the absorbing atom's oxidation state and coordination environment. The XAS spectra can be measured either using a transmission detector, which can then be converted to absorption by comparing energy received as compared to incoming energy, or using a fluorescence detector binned for the appropriate element. Generally in rock samples, X-ray fluorescence is measured since the transmission signal is absorbed by the thick sample and/or glass slide.

There are other, more indirect ways to measure the redox state of manganese, but they either also operate in bulk or do not offer a definitive redox measurement. Titration

methods can give the average redox state of a bulk sample (e.g., Moore et al., 1950), but cannot distinguish mineral host or map redox state at a textural scale. X-ray diffraction (XRD) methods yield the crystal structures present in samples, which can lead to a definitive mineral identification implying redox state, but a bulk XRD measurement cannot show the small-scale relationships between minerals or detect rare and fine-grained or amorphous phases, all of which are vital for understanding the minerals' depositional history. Electron backscatter diffraction (EBSD) on the scanning electron microscope (SEM) can match smaller-scale textures to mineral diffraction patterns, but not all minerals give good diffraction patterns and EBSD is limited by the small area of focus of the SEM. Furthermore, in carbonates (an important phase in ancient manganese deposits), chemical substitution causes variety in mineral structure and ambiguous XRD identifications (Matsumoto, 1992).

Using synchrotron-based X-ray absorption spectroscopy, one can definitively identify mineral host and distinguish redox states clearly by fingerprinting, or comparison to standards (Fig. 2). Bulk powders of the rocks can be measured for overall mineralogy and redox state to extend data to larger scales, but thin sections of the rock can also be produced and analyzed using a spatially-resolved XAS microprobe to understand small-scale relationships. The microprobe can be used to measure X-ray fluorescence for a particular element on a micron scale by rastering the X-ray beam across the sample. X-ray absorption spectra for a particular element can also be obtained at targeted points, providing parallel information on the overall chemistry as well as precise redox and

mineral information. Furthermore, the microprobe can produce ‘redox images’ of a sample by measuring the X-ray fluorescence across a sample at several energies through the absorption edge of interest (Mayhew et al., 2011; Webb, 2011; Johnson et al., 2013). These multiple-energy maps are subsequently reduced by fitting to internal standards to a redox map, thereby creating an image of variations in phase and/or redox state at a $\sim 2 \mu\text{m}$ scale of a given element within a sample.

XRD methods and other light and electron-based microscopy can effectively be used to complement X-ray absorption spectroscopy measurements to produce a thorough understanding of a manganese deposit. Light and electron microscopy are crucial for understanding phase relationships as observations can be made on the same scale as mineralogical textures, allowing one to distinguish more primary minerals from cross-cutting or vein-filling phases. SEMs with an attached X-ray energy dispersive spectrometer (EDS) or an electron microprobe with X-ray wavelength dispersive spectrometers (WDS) measures elemental abundances via characteristic X-ray fluorescence spectra that are suggestive and/or indicative of various minerals.

2.1 Sample acquisition and preparation

We produced ultrathin ($\sim 15 \mu\text{m}$) sections from rock billets cut from each of our study sites and analyzed them using a diversity of methods. Ultrathin sections were made from rock billets by High Mesa Petrographics. For most samples, we also powdered $\sim 200 \text{ mg}$ using a microdrill or an agate mortar and pestle to make a bulk measurement. Samples

were acquired from a variety of sources. The deep-sea manganese nodule was collected from the seafloor surface of the South Pacific Gyre as part of Expedition Knox-02RR in Dec 2006-January 2007. Four samples from the IODP Leg 128 cores held at the Kochi Core Center in Kochi, Japan were acquired by a sample request application. J.B. Maynard, from the University of Cincinnati, graciously donated a variety of his samples from the Molango manganese deposit in Mexico. T. Piacentini, then at University of Queensland-Brisbane, kindly donated one thin section and two powdered samples from the Urucum mine in Brazil for this project. Hotazel samples examined were collected from a well-preserved open mine by T. Raub and J. Kirschvink (Caltech). Koegas samples are derived from the Agouon drilling project and a trip funded by the Lewis and Clark Astrobiology Fund. Kungarra samples were collected by J. Johnson from the Bolgeeda-Turee Creek 'Boundary section' described in Williford et al (2011) during the course of an Agouon-sponsored field research excursion. The relevant geological contexts for each Mn deposit are described in the Results section.

2.2 Analytical methods

We examined our thin sections with transmitted and reflected light microscopy to observe petrographic textures. We used the SEM-EDS to document small-scale relationships between textures and measure elemental distributions and abundances. The Caltech Geological and Planetary Sciences Division Analytical Facility houses a Zeiss 1550VP Field Emission SEM equipped with an Oxford X-Max 80mm² SDD EDS system. We produced high-resolution images in backscatter detector imaging mode to enhance

compositional contrast, as areas with higher average atomic numbers will generate more backscattered electrons. We used EDS to produce point elemental measurements and X-ray maps of regions. Quantitative elemental analysis provides relative accuracy of better than 5%.

We measured these powder and thin section samples at the Stanford Synchrotron Radiation Lightsource (SSRL). We used two imaging beam lines: beam line 10-2 and beam line 2-3. These experimental stations cover a wide range of beam sizes (2-100 microns) and incident X-ray energies (2-20 keV). With beam line 10-2, we use the larger beam size and high photon flux to perform rapid screening of thin sections. These qualities allow us to produce coarse-scale maps of a wide range of samples across the deposit volume, and determine representative domains to target with smaller-scale analysis. Beam line 10-2 maps were generated using a Vortex SII International Silicon drift detector to collect X-ray fluorescence signals for each $\sim 30\text{-}100\ \mu\text{m} \times \sim 30\text{-}100\ \mu\text{m}$ pixel. Subsequently, at beam line 2-3, we mapped chosen regions of interest at four to five energies chosen to have redox- or mineral-distinctive X-ray absorptions (6551 eV, 6557/8 eV, 6562 eV, 6573/5 eV for Mn). These higher resolution maps at $\sim 2\text{-}5\ \mu\text{m}$ were produced with a $2\ \mu\text{m}$ beam using Kirkpatrick Baez mirrors for focusing, with X-ray fluorescence signals collected on a Vortex SII International Silicon drift detector. We measured X-ray absorption near edge structure (XANES) spectra at $2\ \mu\text{m}$ points in these maps to produce internal standards and to confirm best-fit assignments. When available, we additionally measured bulk sample powder at beam line 4-1 to obtain the spectra for

average manganese redox state and mineral phase. At beam line 4-1, we collected X-ray absorption spectra in both transmission and fluorescence mode using a Lytle detector for fluorescence detection. The energy of the experiment was selected using a Si(220) $\Phi = 90$ crystal. We used a collimating mirror to help reduce harmonics in the beam and duplicates were run on all spectra for XANES scanning from 6310 to 7108 eV. Samples were prepared as monolayers of bulk sample powder on tape. All beam lines were calibrated using the pre-edge peak of a potassium permanganate [KMnO₄] standard defined as 6543.34 eV.

After initial observations that we had two end-members in the Mn-carbonate family, we measured XANES spectra of standards of kutnohorite and rhodochrosite. Our rhodochrosite standard from the Pachapaqui District, Peru has a relatively uniform composition averaging Mn_{0.97}Ca_{0.02}Mg_{0.01}CO₃. We had two kutnohorite samples, one from a 5cm crystalline cluster from South Africa and one microdrilled from carbonate nodules with a composition CaMn_{0.7}Mg_{0.3}(CO₃)₂ in the South African Hotazel formation. The kutnohorite crystal cluster had a variable Mn:Ca ratio with some pure calcite but we use a homogenized powder approximated at Ca_{0.63}Mn_{0.36}Mg_{0.01}CO₃ from an average of EDS spectra (chosen from spectra that had measurable Mn since XANES of only Mn will not measure pure calcite). Previous compilations had determined that rhodochrosite was an abundant mineral in many Mn deposits (Maynard, 2010) and kutnohorite also appeared to be an important phase in several ancient deposits of manganese, including the giant Hotazel formation and the Koegas Subgroup in South Africa (Gutzmer, 1996;

Tsikos et al., 2003; Johnson et al., 2013). Our standard spectra and sample measurements highlight the subtle XAS differences between rhodochrosite and a kutnohorite or Mn-bearing calcite. These differences arise from the expansion of the hexagonal unit cell of kutnohorite and calcite (kutnohorite ideally $a = b = 4.850$, $c = 16.340$; calcite ideally $a=b=4.989$, $c=17.061$, crystal cluster standard measured $a=b=4.949$, $c=17.062$) as compared to rhodochrosite (ideally $a = b = 4.7680$, $c = 15.6350$; measured $a=b=4.779$, $c=17.062$), resulting in slightly larger distances from the central Mn to the carbonate groups and tertiary Ca and Mn shell distances. We harnessed these slight XAS differences to map the spatial distribution of these two carbonate types in carbonate-dominated Mn deposits, which enabled us to better understand the primary vs. secondary nature of rhodochrosite and kutnohorite in these formations.

Several sections contained previously unidentified minerals in terms of Mn XAS spectra and X-ray EDS spectra. Two were small Mn(IV) oxides identified from our Hotazel representative section and one was an abundant Mn(II) mineral from our Santa Cruz section. These and other samples were further examined using SEM-based electron backscatter diffraction (EBSD) and on the electron microprobe to quantify elemental abundance. Samples for EBSD measurements were additionally polished using a vibration polisher. EBSD patterns of minerals were indexed using crystal structure databases for identification and/or confirmation of mineral phase. Quantitative measurements of points from manganese-bearing carbonates and from minerals unidentified by XAS spectrometry were made using a JEOL JXA-8200 advanced

Electron Probe Microanalyzer (EPMA). This instrument is part of the Geological and Planetary Sciences Division Analytical Facility and is equipped with five wavelength dispersive X-ray spectrometers (WDS) and a tungsten electron source. The precision for elements were as follows for carbonates: Mn (0.6%), Ca (0.69%), Mg (1.5%), and Fe (1.1%). For Hotazel oxides and the Santa Cruz formation silicate, one-sigma precision was slightly different due to the different minerals: Al (1.9%), Fe (1.7%), Mg (1.7%), Ca (1.1%), Na (5.2%), K (5.3%), Mn (0.27%), and O (0.28%). Detection limits were 0.04 or better for all five elements. The Mn(II) mineral from the Santa Cruz section was further analyzed using Raman spectroscopy, a visible light (514nm) vibrational spectroscopic technique that probes molecular symmetry, using the Raman detector in the Mineralogy lab at Caltech.

3. RESULTS

We have chosen a range of manganese deposits, from a variety of paleoenvironments and geologic intervals, to capture the mineralogical and textural diversity of manganese-enriched formations (Fig. 1, arrows). While there is significantly more mineralogical richness associated with hydrothermal and metamorphic manganese deposits, we focused this study on the best-preserved samples we could acquire from each of these deposits. We note that nearly all ancient rocks have been affected by late diagenetic, metamorphic, and metasomatic processes, and our observations highlight the key changes that have taken place. With that in mind, by combining traditional sedimentology and advanced

microscale techniques, we can piece together a common paragenetic sequence of mineral formation in Mn-rich sediments.

Modern manganese deposits and manganese-enriched rocks from 3 million years ago to 2415 million years ago were probed for overall manganese redox state, and meso- and micro-scale manganese mineral relationships. In seeking to understand the processes that alter manganese minerals through time, we developed efficient strategies to understand manganese mineralogy using synchrotron-based methods and synthesized a theory of manganese stabilization in the rock record. We also made fundamental observations documenting the important reduction processes that occur in ancient manganese deposits, as all ancient deposits are significantly more reduced (Mn(II) or Mn(II/III) phases) than modern deposits (Mn(IV) phases). See Table 1 for a summary of our results.

3.1 Modern manganese deposits

Our calibration point for ‘modern’ manganese deposition was a deep-sea manganese nodule collected from the ocean floor. The deep-sea manganese nodule (Fig. 3) was collected from the ocean floor in the South Pacific Gyre, an extremely oligotrophic area of the ocean where sedimentary organic fluxes are low and pore fluid oxygen levels remain high – within 150 to 250 μM of O_2 (Ingle et al., 1990).

The textures of this deep-sea manganese nodule, best observed under SEM, are quite striking (Fig. 3). The manganese presents as thin layers of isopachous cements with

abundant inclusions of aluminosilicate detrital minerals that together manifest in a stromatolitic morphology. Brighter manganese oxide bands alternate with mixed manganese and iron oxides, and on a micron-scale, the bands vary from finely laminated to porous (Fig. 3). The manganese oxide phases are sub-micrometer disordered material intermixed with other phases in a replacive texture, and they generate no EBSD pattern as they are either amorphous or too finely crystalline to produce a discernible diffraction pattern.

By synchrotron analyses, the entire nodule consists of solely Mn(IV) oxides. Bulk samples and thin sections of all these modern-day manganese deposits were imaged using synchrotron-based redox and mineral mapping (Fig. 4). Fig. 4 shows manganese abundance as mapped on beam line 10-2 and reduced from multiple energy maps using fitting to produce a manganese redox map (see Methods). We also mapped smaller, representative areas at beam line 2-3 at a higher resolution and measured X-ray absorption spectra of specific points. X-ray absorption spectra from points and bulk powders are shown on the right with the most similar standard spectra. For this modern manganese deposit, birnessite was the best spectral match, and both redox mapping and point spectra indicate that manganese is dominantly present as Mn(IV) oxides. Others (Bargar et al., 2000; Tebo et al., 2004; John R. Bargar et al., 2005; S. M. Webb et al., 2005) also determined that birnessite was the dominant oxide formed by manganese oxidation, and we therefore concur that birnessite is the stable Mn oxidation product.

3.2 Ancient manganese deposits

While Mn(IV) oxides appear to be the primary Mn phase entering sediments, we consistently observe that Mn is converted to other phases by diagenetic (secondary) processes. To explore how manganese ends up stabilized in the rock record and probe which processes have affected the Mn mineralogy, we examined five Mn-enriched sedimentary deposits ranging from relatively recent material in ocean drill cores (3 million years ago) to the earliest large deposit of Mn in the rock record (2.4 billion years ago). Most of these ancient deposits are significant terrestrial Mn ores and are highlighted in Fig. 1. These Mn deposits not only cover an enormous expanse of time, but they also capture a variety of both modern and ancient environments: samples were acquired from South Africa, Brazil, Mexico, and the Japan Sea, and their environments have been reconstructed as varying from shallow marine to continental rift basin to deep ocean trench. Surprisingly, this diversity of Mn deposits displays relatively few predominant minerals, suggesting the operation of common and widespread diagenetic processes in Mn-rich sediments. Beginning with the most recent deposit and proceeding back through time, we describe the geologic setting, visual and electron microscopic observations, and finally the X-ray absorption measurements for each of these deposits.

3.2.1 Japan Sea Drill Core

We studied materials from an ODP Site 799 core drilled in the Japan Sea that had reported high manganese levels from intervals > 50 meters below sea floor (Matsumoto,

1992). This ODP core was drilled into the Kito-Yamato trough, an organic carbon-rich deep trench formed as a failed rift basin in the center of the Japan Sea (Matsumoto, 1992). The sediments contain a suite of unusual diagenetic carbonates, including lansfordite (a hydrated magnesium carbonate), magnesite, and rhodochrosite, as well as calcite and dolomite. Rhodochrosite was reported in Quaternary to Miocene-aged rocks, especially abundant in Pliocene and upper Miocene sediments and interpreted as diagenetic. Calcian (22.5-38.5% Ca) rhodochrosite microspherules, about 2 to 12 μm in diameter, were described as filling interstices of the matrix (Matsumoto, 1992). This sedimentological description and the depleted carbon isotopes (-4 to -15 ‰, reflecting incorporation of organic carbon-derived CO_2) implies that the rhodochrosite was secondary (Matsumoto, 1992). Matsumoto (1992) observed several micrometer-sized high-backscatter (high molecular weight) spots in the rhodochrosite that he was unable to identify as either iron sulfides, or manganese or iron oxides (Matsumoto, 1992).

To examine the petrogenesis of manganese in this deposit, we acquired several samples from this core. Three samples (196m, 326m, 502m, Pliocene to late Miocene in age) were unlithified, but the deepest sample at 533m (from the Late-Middle Miocene boundary, approximately 11 million years ago) was sufficiently consolidated enough to make a thin section. Our thin section of core material at 533m had tan and darker brown carbonates with scattered opaque minerals (Fig. 5). The top of the section was dominated by darker carbonates while the bottom half had a higher abundance of lighter tan carbonates but both were patchily distributed throughout the section (Fig. 5). SEM observations

indicated that the tan carbonates were coarsely crystalline ferrous magnesium carbonates, which appear yellow-orange under transmitted light and a slightly darker grey in SEM photos. These are labelled $(\text{Mg,Fe})\text{CO}_3$ but this represents a range of EDS measurements, which were $\text{Mg}_{0.37-0.44}\text{Fe}_{0.32-0.37}\text{Mn}_{0.1-0.17}\text{Ca}_{0.09-0.14}\text{CO}_3$. These coarse magnesian crystals have brighter rims, which we measured to be iron-enriched, with formulas of $\text{Fe}_{0.44-0.52}\text{Mg}_{0.22-0.25}\text{Mn}_{0.15-0.21}\text{Ca}_{0.08-0.11}\text{CO}_3$. The top half of the sample and a spot at the bottom, which appear darker brown in transmitted light and brighter grey in SEM photos, are much more manganese-enriched, and these areas have clusters of finer-grained calcium and manganese carbonates. In the top half of the section, we observed manganoan calcium carbonate similar to kutnohorite with a formula of $\text{Ca}_{0.38-0.52}\text{Mn}_{0.29-0.41}\text{Mg}_{0.12-0.19}\text{Fe}_{0.03-0.06}\text{CO}_3$. These finer-grained carbonate clusters were surrounded by the coarser-grained magnesian carbonates (Fig. 5). Upon close examination, the small dark brown spot at the bottom of the section is a combination of high-backscatter and low-backscatter minerals. Indeed, we found examples of both crystalline and finer-grained kutnohorite-like carbonates similar to the top half of the section, but these display rims and crystalline masses of a calcian rhodochrosite as well. This rhodochrosite had a formula range of $\text{Mn}_{0.68-0.74}\text{Ca}_{0.21-0.25}\text{Mg}_{0.03-0.05}\text{Fe}_{0.01-0.02}\text{CO}_3$. Both cross-cutting relationships and the finest-grained carbonates imply that the manganoan calcium carbonate phases were produced early during sedimentary diagenesis, suggesting the precipitating fluids were both calcium- and manganese-rich. The coarser ferrous magnesium carbonate crystals that suggest later recrystallizing fluids were magnesium and iron rich, and the bright iron-rich rims of these crystals point to an even later introduction of more iron-enriched fluids.

The rhodochrosite too appears to be tied to later diagenetic processes, either from manganese-rich fluids or recrystallization and redistribution of calcium and manganese from earlier manganoan calcite precipitates.

We measured all four samples for bulk powder XAS and mapped the thin section sample at 533m for manganese mineralogy and redox information (Fig. 6). One sample, IODP 326m, had a very weak absorption signal due to very low levels of manganese, and the spectra was difficult to identify besides observing a Mn(II) peak. The other samples were more clearly associated with the Mn-rich carbonate zones previously described (Matsumoto, 1992). The sample at 196m contains a mixture of kutnohorite ($\text{Ca}_{0.5}\text{Mn}_{0.5}\text{CO}_3$) and rhodochrosite (MnCO_3), best fit by linear combination to 58% kutnohorite and 42% rhodochrosite. At 502m, the kutnohorite influence on the spectra had decreased, with the fit yielding an estimate of 54% kutnohorite and 46% rhodochrosite. By 533m, the bulk spectra was fit by 52% kutnohorite and 48% rhodochrosite. It is notable that the rhodochrosite appears to be increasing with depth, suggesting that a greater degree of burial induces rhodochrosite replacement of kutnohorite. By X-ray mapping, manganese was present exclusively as Mn(II) in different carbonate phases; the bright minerals observed previously (Matsumoto, 1992) were iron sulfides, not Mn oxides. Multiple-energy X-ray fitting showed a dominance of kutnohorite-like carbonates from the top of the section, similar to results from the SEM (Figs. 5 and 6), and a mixture of rhodochrosite and kutnohorite from the bottom manganese-enhanced spot. This hot spot shows a similar mixed pattern of rhodochrosite

and kutnohorite in both light and dark grey backscatter on the SEM and the mapped kutnohorite/rhodochrosite distribution from XAS.

3.2.2 Mexican Molango Deposit

The largest manganese deposit in North America is the Upper Jurassic-age (~155 Ma) Molango deposit in Mexico. During this time, Mexico's large rift basins had become open to marine waters and had developed a carbonate platform-shelf, lying behind a trough-island arc system (Scott, 1984). The manganese enrichments are hosted by marine limestone and have been determined to be primarily in rhodochrosite and kutnohorite, with the Mn ore zone directly overlying a black calcareous shale (Okita et al., 1988; Okita and Shanks, 1992). Okita et al (1988) proposed that the stratiform, laminated manganese-bearing carbonates formed from the diagenetic reduction of manganese oxides by organic carbon—a hypothesis supported by ^{13}C -depleted carbon isotopic data from the Mn-enriched carbonates. Dispersed organic matter occurs throughout the manganese ore bed, suggesting that manganese oxide reduction had occurred in pore waters (Okita et al., 1988). The isotopic composition of the Mn-carbonates reflects a mixture of seawater and dissolved inorganic carbon (DIC) produced from the respiration of organic carbon; measured rhodochrosite carbon isotopes average at -13 per mill and kutnohorite carbon isotopes covary systematically from -7 to 1.7 per mill with decreasing Mn content (Okita et al., 1988).

We examined a variety of samples from the Molango deposit via X-ray analyses and microscopy. Looking at the microscale textures of one sample [Aco 2.4m, all rhodochrosite by XAS], we found blocky crystals of ferrous rhodochrosite ($\text{Mn}_{0.69}\text{Fe}_{0.16}\text{Ca}_{0.1}\text{Mg}_{0.04}\text{CO}_3$), potential dark grey pockets of the original matrix ($\text{Ca}_{0.55}\text{Mn}_{0.24}\text{Fe}_{0.14}\text{Mg}_{0.07}\text{CO}_3$), and bright white rhodochrosite cements (bright white, $\text{Mn}_{0.93}\text{Ca}_{0.06}\text{Fe}_{0.01}\text{CO}_3$) (Fig. 7). Although the highly recrystallized nature of the Molango deposit makes observing consistent cross-cutting relationships challenging, the extremely high Mn (24 to 93% of cations) content of the cements suggests the secondary precipitation enriches carbonates in Mn, and that perhaps the calcian carbonates reflect the earliest sedimentary phase. We measured XAS spectra on seven samples from throughout the Molango deposit from the Tetzintla section (T1) and the Acoxcatlan section (Aco) (Okita and Shanks, 1992) (Fig. 8). These showed rhodochrosite in the 0-9m range, where the Mn ore zone is located (Okita and Shanks, 1992), transitioning to a mixture of kutnohorite (71%) and rhodochrosite (29%) at 19m and then only kutnohorite well above the ore zone. We also mapped three representative thin section samples in detail for redox state and speciation on the X-ray microprobe (Fig. 8). These samples are dominantly rhodochrosite with small patches of kutnohorite in ore zone samples (Aco 0m and 2.4m, Fig. 8), consistent with observations from the SEM-EDS. When mapping for carbonate speciation in overlying non-ore samples, we found dominantly kutnohorite (T1 26.5m, Fig. 8), similar to previous results (Okita et al., 1988; Okita and Shanks, 1992). The highly recrystallized nature of the ore zone sample (Fig. 7) indicates that the ore zone may have undergone significant hydrothermal or metamorphic alteration.

3.2.3 Brazilian Santa Cruz deposit

During the extreme Neoproterozoic glaciations, significant iron-and-manganese formations were deposited on several cratons (Hoffman and Schrag, 2002; Klein, 2005). One iron-manganese deposit from Brazil was described early on as the “youngest” banded iron formation remarkably enriched in manganese, from 27% to 45% Mn by weight (Urban et al., 1992). This deposit, in the Santa Cruz Formation, has age constraints between 889 ± 44 Ma and 587 ± 7 Ma (Hasui and Almeida, 1970; Piacentini et al., 2013) and is associated with diamictites. It is located in the Jacadigo Basin, an ancient continental rift basin that records the transition from clastic basin fill to lacustrine or marine gulf deposits that include iron and manganese formation and carbonate deposits (Freitas et al., 2011). While most authors consider the oversized clasts in the manganese and iron deposits as dropstones from glacial retreat (e.g., Urban et al., 1992; Klein and Ladeira, 2004), these have also been interpreted as rift-related mass flow deposits (Freitas et al., 2011).

Despite the still-contentious regional tectonics of the Jacadigo Basin, the Santa Cruz formation has been better studied in terms of manganese and iron mineralogy. There are four separate Mn-rich intervals throughout the formation, with manganese occurring as nodules, as cements around clastic detritus, and as massive sedimentary horizons, separated by ferruginous sandstones and hematite jaspelites (Urban et al., 1992). Urban et al. identified cryptomelane, a K-bearing manganese oxide [$\text{KMn(IV)}_6\text{Mn(II)}_2\text{O}_{16}$], as the

dominant manganese mineral, but also found braunite $[\text{Mn(III)}_6\text{Mn(II)O}_8\text{SiO}_4]$ and noted that braunite was replaced by cryptomelane and pyrolusite, another Mn(IV) oxide mineral $[\text{Mn(IV)O}_2]$. They found other accessory manganese minerals like lithiophorite $[\text{Mn(IV)(Al,Li)O}_2(\text{OH})_2]$, manganite $[\text{Mn(III)OOH}]$, and fissure-associated metamorphic minerals such as Mn-rich amphiboles and nambulite $[\text{LiMn(II)}_4\text{Si}_5\text{O}_{14}(\text{OH})]$ (Urban et al., 1992). Later, Klein and Ladeira (2004) also described another manganese-bearing mineral from this deposit as manganoan dolomite, which they found in both the iron and manganese layers.

While the best manganese ore comes from surface-weathered supergene caps or hydrothermally-altered zones along faults (Klein and Ladeira, 2004), we focused on well-preserved underground samples, since weathering horizons in this area are very deep (Vasconcelos, 1999). We obtained one thin section sample and two bulk powder samples from the Brazilian Santa Cruz Formation. The thin section sample (SD92.11) came from over 2.5 km into an underground manganese mine at Urucum, and was collected away from faults or exposed surfaces. Thus, it provides a well-preserved example of the Santa Cruz Fm mineralogy. It is derived from the second stratigraphic manganese layer (Mn 2), which is the largest of the four layers (Urban et al., 1992). Another sample, a powder sample also from the second manganese layer (SD92.07), was collected ~1km into the Urucum underground manganese mine, but along a fault.

SEM observations of the manganese-rich strata from the Santa Cruz Formation reveals that even the best-preserved materials contain a remarkably complex (compared to other deposits) assemblage of Mn minerals. While braunite ($\text{Mn(III)}_6\text{Mn(II)SiO}_{12}$), rhodochrosite, and kutnohorite are present, and confirmed via EBSD (Fig. A1), there were other Mn minerals that were more difficult to identify (Fig. 9). In bulk XAS, the sample from the fault zone best matched cryptomelane, confirming that this is a prevalent mineral in the formation and suggesting that the faults through the Santa Cruz Formation have introduced oxidizing fluids to the rock surrounding the faults. However, the subsurface sample collected away from the surface and any faults was composed of only Mn(II) and Mn(III) minerals by X-ray mapping, with four distinctive minerals identified using our point spectra (Fig. 10). The Mn(III) minerals are mainly braunite [$\text{Mn(III)}_6\text{Mn(II)O}_8\text{SiO}_4$], but the Mn(II) minerals consisted of kutnohorite, rhodochrosite, and another spectra we could not identify based on our standard suite (Fig. 2). We examined this phase using EBSD but found it was amorphous or too finely grained to generate a diffraction pattern. Textural observations indicated that this is a late-stage metamorphic phase, as it had a webbed and fibrous texture and appeared to be growing on and replacing kutnohorite (Fig. 9). By electron probe, we were able to identify that this mineral had a formula of approximately MnSiO_3 , with 44.8% MnO, 35.6% SiO_2 , 4.9% Al_2O_3 , 2.28% FeO, 2% MgO, 0.5% Ca, and either water or hydroxide groups. This is a good fit for caryopilite, but could be either caryopilite or kellyite, which are both metamorphic manganese silicates. We further examined the mineral using Raman

spectroscopy and found that the best match was caryopilite (using the online RRUFF database). Kellyite has a completely different structure and Raman spectrum (Fig. A2).

3.2.4 South African Hotazel Formation

The enormous *circa* 2.2 billion-year-old manganese deposit within the Hotazel Formation in the ancient Kaapvaal Craton of South Africa is a marine sedimentary deposit consisting of interbedded manganese-rich and iron-rich rock strata (Gutzmer, 1996). The timing of its deposition—soon after the first ‘great’ rise of oxygen—has invoked the hypothesis that the deposit might be recording interactions between the newly sourced O₂ and the iron- and manganese-rich ocean (Kirschvink et al., 2000). The Hotazel Formation was deposited in a marine setting, either in a back-arc setting with a distant volcanic source (Beukes, 1983) or a proximal mid-ocean ridge environment (Cornell and Schütte, 1995). Jaspilitic iron formation and manganese intervals overlie the subaqueous Ongeluk basalts and then transition into the Mooidrai Formation carbonate platform, which progrades across the basin from east to west (Gutzmer, 1996; Kirschvink et al., 2000). The three manganese ore units have been well-characterized as mineralogically braunite and kutnohorite (Gutzmer, 1996; Tsikos et al., 2003), but highly altered and hydrothermal regions of the Hotazel Formation have exotic minerals and spectacular gemstones (Cairncross and Beukes, 2013).

Electron and X-ray analyses of the Hotazel samples indicate that these two minerals—braunite and kutnohorite—are pervasive, but we observed several other interesting

minerals as well. From our SEM imaging of samples from the Hotazel manganese formation, it is clear that braunite crystals cross-cut kutnohorite, indicating that kutnohorite was an earlier phase as compared to the braunite (Fig. 11). There is a recrystallized Mn-calcite phase (with about 10% Mn) that too cross-cuts the kutnohorite (Fig. 11). Micron-sized iron oxides appear to have precipitated even later than the braunite, as their mineral boundaries cut into braunite (Fig. 11, matrix). Using SEM-EDS, we observed several Mn or Mn-Fe oxides that did not appear to contain silicon, but we could not determine the mineralogy of these phases.

At the synchrotron, we measured braunite and kutnohorite by XAS on micromilled (bulk) powder from the dark matrix and bright white nodules of the Hotazel, and used X-ray mapping to confirm that braunite and kutnohorite dominate the deposit. However, X-ray mapping also indicated the presence of rare Mn(IV) oxide minerals that coincided with the silicon-free oxides we had observed on the SEM. Texturally, these Hotazel Mn(IV) minerals are very different from the modern manganese nodule oxides (Fig. 12) (or the surface-weathered samples of Kungarra Formation and Koegas Subgroup discussed in section 3.3), which appear fuzzy and soft. Instead, these Hotazel Mn oxides have a hard, mineralized texture. Several of these Mn(IV) oxides appear to be fibrous and are related to cross-cutting veins, and are likely related to later oxidizing fluids (Gutzmer, 1996) (Fig. 12). However, two of the discovered Mn(IV) oxide minerals are more consistent with an early inclusion, or unreacted residue, of original sediment. One banded manganese oxide is cross-cut by two generations of kutnohorite and by a braunite crystal,

implying that it was present in the sediments earlier than all three of these phases (Fig. 11). Another is a Mn and Fe oxide which is also cut by Mn-carbonate precipitates. We examined the two Mn(IV) oxide types, one fibrous and one layered manganese oxide (not mixed Mn-Fe oxide), using electron backscatter diffraction (EBSD) on the SEM, and found that they were crystalline but poorly matched by standard spectra. E-probe measurements of these two oxide types determined that the composition of the fibrous oxide is $\text{Mn}_{0.84}\text{Na}_{0.04}\text{Ca}_{0.03}\text{Fe}_{0.02}\text{O}_2$ and the potential early inclusion is $\text{Mn}_{0.85}\text{Na}_{0.05}\text{K}_{0.04}\text{Fe}_{0.03}\text{Ca}_{0.03}\text{O}_2$.

3.2.5 South African Koegas Subgroup

Also on the western side of the Kaapvaal Craton, there is an older manganese-enriched suite of rocks in the Koegas Subgroup of the Transvaal Supergroup. The Koegas strata are composed of mainly deltaic and near-shore marine siliciclastics intermixed with banded and granular iron formation, with a paleoenvironmental gradient from proximal to distal (broadly east to west). Manganese enrichments occur in clastic-starved intervals of iron formation deposition (Schröder et al., 2011; Johnson et al., 2013; Johnson et al., 2014). This Koegas Subgroup manganese deposit has been shown to pre-date the rise of oxygen and thus the manganese oxidation mechanism was inferred to be a manganese-oxidizing photosystem prior water-oxidizing photosynthesis (Johnson et al., 2013). From examining two drill cores (GEC and GTF) drilled as part of the Agouron Drilling project, the manganese in the Koegas Subgroup was determined to be hosted entirely by Mn-bearing carbonates (Johnson et al., 2013).

With a manganese-enriched core sample from the Koegas Subgroup (11.6% MnO in bulk, Johnson et al, 2013), we focused on manganese-enriched carbonate nodules with clear compositional variations to examine the relationships between the different major Mn-bearing carbonate phases in the Koegas samples. While most core samples had micron-scale mixtures of Ca-Mn carbonates and Fe-Mn carbonates, a sample from core GTF at 230m shows discrete zonation of these minerals in carbonate nodules with signs of differential compaction. We measured the two carbonate endmembers, shown in SEM photos as bright white-grey (high backscatter) and darker grey (low backscatter), on the E-probe to measure exactly what these two minerals were and determined that they were composed of a $\text{Mn}_{0.41}\text{Fe}_{0.41}\text{Mg}_{0.14}\text{Ca}_{0.04}\text{CO}_3$ (average of white-grey carbonate) and $\text{Ca}_{0.48}\text{Mn}_{0.20}\text{Fe}_{0.18}\text{Mg}_{0.15}\text{CO}_3$ (average of dark grey carbonate) using 18 data points from all three nodules (Fig. 13). While these minerals are not strictly rhodochrosite nor kutnohorite, they comprise a solid solution between ferroan rhodochrosite, manganian siderite, and manganian calcite. All the carbonate phases in this sample appear to have been “ankeritized”, with 14 to 15 cation percent magnesium (Fig. 13).

We measured manganese and calcium abundance by XRF at the synchrotron to isolate the ‘rhodochrosite-like’ and ‘kutnohorite-like’ endmembers for further measurements. The general trends of Mn and Ca concentrations obtained from synchrotron based microprobe observations are consistent with the E-probe measurements and backscatter-highlighted compositional differences. Microprobe XAS spectra through the Ca-rich and

Mn-rich portions of the nodule show dramatic changes, with kutnohorite spectra correctly corresponding to the kutnohorite-like Ca-rich portions of the nodules and rhodochrosite spectra corresponding to the rhodochrosite-like Mn-rich areas (Fig. 14). We were able to map these two carbonate endmembers to indicate their discrete geographical distribution (Fig. 14). With the extent of recrystallization present in the Koegas, it is not possible to conclusively determine whether the manganoan siderite or the manganoan calcite is more primary (Fig. 13).

3.3 Surface-weathered deposits

Many manganese deposits are not studied from core or mine samples, but instead from outcrop samples. While we are primarily interested in understanding the Mn mineralogy of diagenetically stabilized deposits and how these phases reflect processes during and after lithification, we also wished to understand how surface weathering changes the redox state and mineralogy of manganese deposits. We collected samples from three outcrop sites, two of which we also have studied in drill core or mine exposures for primary mineralogy, and we will compare the chemistry of Mn here to our more pristine samples.

From the Santa Cruz Formation manganese deposit, we obtained a sample (SD11.08) from a near-surface sample of the fourth manganese layer (position shown in Piacentini et al, 2013). This sample represents a supergene, oxidized example of a similar provenance but with different preservation conditions for the Santa Cruz Fm than for the

thin section sample previously discussed. The best fit for the spectrum from this sample measured in bulk powder was cryptomelane, identical to what was obtained from the fault-associated sample. This mineralization is likely associated with supergene enrichment and oxidative weathering of the more reduced manganese minerals from this deposit (Urban et al., 1992) (Fig. 10).

We also examined a sample from the 2.415 Ga Koegas Subgroup collected from surface outcrops near Rooinekke, which can be correlated to core samples. The outcrop sample comes from the thin microbialite and grainstone interval in the Rooinekke Formation of the Koegas Subgroup, which has intraformational grains of Mn- and Fe-bearing carbonate (see GTF 63.86m in Fig. 2 of Johnson et al, 2013). High-resolution SEM imaging showed that sub-micrometer Mn oxides intermixed with other phases in a replacive texture without a diffraction pattern (Fig. 15). The surface-weathered sample similarly shows discrete, but random, Mn-enriched zones, and the XAS measurements are most similar to the Mn(IV) oxides cryptomelane or birnessite (Fig. 16). EDS measurements show peaks of potassium and calcium but no sodium—which may be more consistent with Ca-enriched cryptomelane rather than birnessite. Like the Santa Cruz Formation sample, surface weathering again seems to have oxidized Mn(II) carbonate minerals to Mn(IV) oxides and destroyed textural information.

A sample from the Paleoproterozoic-age Kungarra Formation in Australia represents the third highly weathered manganese location. This sample comes from a thin sedimentary

bed with 7% Mn just above the lower contact with the Bolgeeda Iron Formation (Williford et al., 2011). The original mineralogy is unknown, and the age constraints on the Proterozoic deposit are similarly uncertain. The Kungarra Mn horizon appears to be younger than 2449 +/- 3 Ma (Barley et al., 1997) and older than overlying 2209 +/- 15 Ma Cheela Springs Basalt (Martin et al., 1998) and older than intruding mafic sills dated at 2208 Ma +/- 15 Ma (Müller et al., 2005). Detrital zircons in the Kungarra Formation restrict the depositional age to younger than 2420 Ma (Takehara et al., 2010). Thus, the Kungarra deposit may be a contemporary deposit to the Koegas strata, or it may be better correlated to the 2.2 Ga South African Hotazel manganese deposit. We note that the Hotazel deposit does lie above glacial deposits similar to the Kungarra Formation (Williford et al., 2011), but the Hotazel is significantly more Mn-enriched (up to 38% in well-preserved examples) than the Kungarra deposit, which only has 7.4% Mn (Williford et al., 2011), more similar to the Koegas manganese levels.

Light and electron microscopy of the Kungarra manganese-rich bed shows textures similar to the Koegas weathered samples that indicate Mn oxide replacements, and no EBSD pattern could be generated as the crystals are likely too small (Fig. 17). X-ray absorption spectroscopy indicates that the sample is universally Mn(IV) oxides, again either fitting birnessite or cryptomelane (Fig. 18). From the potassium and calcium in EDS measurements, this mineral is potentially cryptomelane ($\text{KMn(IV)}_7\text{Mn(III)O}_{16}$), a common supergene product of Mn oxidation (Urban et al., 1992). The massive, fibrous texture of the Mn(IV) oxide shown by SEM (Fig. 17) highlights that the Mn(IV) is

plainly secondary, likely enriched from original Mn-bearing minerals but possibly introduced by hydrothermal or other fluids.

These three examples indicate that while the kinetics of manganese oxidation may be slow (Morgan, 2005), the exposure to oxygen during long intervals integrated by weathering is effective at oxidizing all lower valent minerals to Mn(IV) oxide phases, and at the same time alters the primary textures.

4. DISCUSSION

From our survey of the mineralogy, textures, and chemistry of manganese deposits, we can divide our observations into three categories: 1) manganese deposits composed of essentially all Mn(IV) oxides, such as the modern seafloor manganese nodules or surface-weathered manganese deposits, 2) deposits where the Mn is found exclusively in Mn(II) carbonates, such as the Koegas deposit, the Molango deposit, and the IODP deposit, and 3) deposits with subequal mixtures of Mn(II)- and Mn(III)-bearing minerals like in the manganese-rich intervals in the Hotazel deposit and the Santa Cruz Formation.

In marine and lacustrine sediments manganese oxidation processes form Mn(IV)-dominated oxides like birnessite (Fig. 3; (Murray et al., 1985; Wehrli et al., 1995; McKeown and Post, 2001; Tebo et al., 2004) and the reduction of these oxides produces Mn-carbonates (Thamdrup et al., 1993; Calvert and Pedersen, 1996; Fischer et al., 2008;

Ying et al., 2011; Lee et al., 2011). Mn oxidation does appear to yield a Mn(III) intermediate that is observable as a short-lived (but potentially important) redox player in suboxic environments (Madison et al., 2013). However, it is not common to observe substantial accumulation of Mn(III) species because they typically disproportionate to Mn^{2+} and Mn(IV) oxides or are subsequently fully oxidized to Mn(IV) oxides that are added to the sediments (Perez and Jeffries, 1992; Wariishi et al., 1992; Samuel M. Webb et al., 2005; Anderson et al., 2009; Learman et al., 2011; Hansel et al., 2012). Reduction of Mn(IV) oxides also may proceed through a short-lived Mn(III) intermediate (Lin et al., 2012), but again, the final product of manganese reduction is Mn^{2+} (Lovley and Phillips, 1988; C.R. Myers and Nealson, 1988; Aller, 1990; Van Cappellen et al., 1998; Thamdrup et al., 2000). Thus the widespread observation of non-transient but stable and abundant Mn(III) phases in the rock record, as documented by this study and others (Gutzmer, 1996; Tsikos et al., 2003; Roy, 2006; Maynard, 2010), is intriguing and indicative of post-depositional processes.

Indeed, all the manganese from well-preserved samples of ancient deposits, whether 3 million years old or 2.2 billion years old, are all more reduced than the modern Mn-rich surface sediments (with the notable exception of rare MnO_2 inclusions in some early diagenetic Hotazel kutnohorite nodules). These observations illustrate that there are common and effective post-depositional reduction processes that convert the Mn(IV) precipitates in sediments to Mn(II) and Mn(III) minerals during early and late diagenesis. Using micro-scale observations of mineralogy and chemistry tied to petrographic

textures, we can ordinate these different phases and develop a general framework for how post-depositional processes impact manganese mineralogy and redox state and determine a paragenetic sequence of manganese minerals.

4.1 Paragenetic model

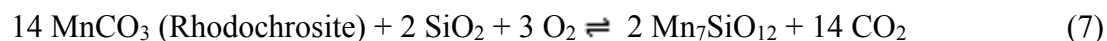
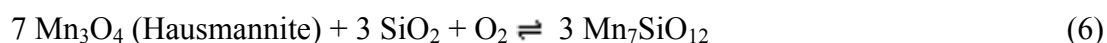
The first precipitates to enter and concentrate Mn in sediments are Mn(IV)-dominated oxides. The deep-sea manganese nodule from the seafloor being fully comprised of Mn(IV)-dominated oxides lends support to this, as well as other reports of Mn(IV) oxides being the dominant precipitate produced by manganese oxidation (e.g., Tebo et al., 2004). The discovery of Mn(IV) oxide inclusions, which we propose is a primary residue from the original sedimentary precipitates on the basis of petrographic textures, is an additional line of evidence suggesting that these manganese deposits began as Mn(IV)-dominated oxides. The weathered samples of Mn-bearing rocks confirm that when oxygen is present for a sufficient amount of time, manganese seems to be dominantly oxidized and stabilized as Mn(IV)-oxide phases.

The precipitation of Mn(II)-bearing carbonates from the reduction of Mn(IV) oxides by organic carbon has been inferred previously from observations of the geologic record (Okita et al., 1988; Tsikos et al., 2003). Often, the diagenetic reaction is presented similar to Reaction (4), implying that rhodochrosite, or MnCO_3 , is the reaction product. However, we document in several formations (see the Koegas, Molango, Urucum, and Hotazel deposits) the priority of kutnohorite ($\text{Mn}_{0.5}\text{Ca}_{0.5}\text{CO}_3$). This calcium manganese

carbonate precipitation is also promoted from similar Mn(IV) reduction reactions described in (3) but the precipitating carbonate incorporates Ca abundant in pore fluids. As discussed above, these manganese reduction reactions occur by interaction of microbes and solid Mn(IV) oxides in the absence of oxygen. While manganese reduction does take place in anoxic waters, such as the Black Sea, the Mn(II) produced is diluted into the surrounding water column, and does not sufficiently increase in concentration to form Mn-carbonates (Calvert and Pederson, 1996). Thus, the production of Mn-carbonates post-Mn(IV) reduction likely only takes place in porewater-filled cavities of anoxic sediments enriched in “trapped” manganese oxides (Calvert and Pedersen, 1996). Marine sedimentary porewater is Ca-rich at ~10.5 mM (Wenzhöfer et al., 2001; Rao et al., 2012), and increasing the Mn²⁺ concentration of seawater promotes the precipitation of carbonates with kutnohorite-like composition. Bottcher (1998) precipitated calcium-manganese carbonates at 20, 60, and 90°C, and the carbonate precipitates had a manganese composition that was enriched but related to the Ca:Mn concentrations. Similarly, Mucci (2004) synthesized a calcian rhodochrosite by combining equal molar solutions of Ca and Mn. He demonstrated that either manganoan calcite or calcian rhodochrosite will form depending on the porewater Mn:Ca concentrations, calcite surfaces, and reaction kinetics (Mucci, 2004). Thus in the presence of high porewater Ca levels (i.e., seawater compositions), manganese oxide reduction promotes the precipitation of carbonates with subequal amounts of Mn and Ca, as opposed to endmember carbonates like rhodochrosite (MnCO₃).

Mn-bearing carbonates from a variety of unlithified sediments are invariably mixed Mn-Ca(+/-Mg) carbonates rather than endmember rhodochrosite, including sediments in the Baltic Sea, Panama Basin, Loch Fyne, among other locations (Calvert and Price, 1970; Pedersen and Price, 1982; Jakobsen and Postma, 1989; Calvert and Pedersen, 1996). Modeling the precipitation dynamics similarly results in formation of kutnohorite or calcic-rhodochrosites depending on Mn concentration, and rhodochrosite is not a stable phase in reasonable porewater compositions (Middelburg et al., 1987). Since all of our examined sedimentary deposits are marine in origin, and it is unlikely that Ca levels in the oceans have changed so substantially since Archean time (Grotzinger and Kasting, 1993; Lowenstein et al., 2001; Fischer et al., 2009), the early diagenetic carbonate precipitate of all of these deposits was likely kutnohorite. Rhodochrosite, then, either forms in Ca-depleted porewaters (which seems unlikely) or more probably as a secondary carbonate associated with dissolution and higher temperature re-precipitation of carbonate closer to endmember MnCO_3 . Carbonate mineral textures from light and electron microscopy (e.g., Figs. 5, 7, 13) demonstrate substantial amounts of carbonate diagenesis—recrystallization and precipitation of secondary and tertiary cements that are commonly chemically zoned. It is also interesting, and perhaps illuminating, that the Mn(IV) oxide inclusion in the Hotazel formation occurs occluded by kutnohorite nodular cements, not rhodochrosite. These textures imply that kutnohorite is commonly an earlier diagenetic precipitate rather than rhodochrosite.

Textural observations of the Mn(III)-rich phase braunite from the Hotazel and Santa Cruz formations indicate that it formed after kutnohorite, but still early in diagenesis as the braunite is generally fine-grained and defines sedimentary lamination. Yet the timing and formation process of braunite during diagenesis and/or metamorphism is unclear (Robie et al., 1995). The composition of braunite is related to the manganese(III) oxide bixbyite ($\text{Mn(III)}_2\text{O}_3$), but with substitution of Mn^{2+} and Si^{4+} for 2Mn^{3+} . Interestingly, the Si content of braunite appears to be relatively invariable with metamorphic grade (Abs-Wurmbach, 1980). Braunite has not been synthesized in the laboratory, but there are several proposed mechanisms for its formation (Robie et al., 1995); we highlight those with plausible initial conditions for marine sediments (e.g., rhodonite, a high-temperature metamorphic Mn(II) silicate is not a likely precursor precipitate):



We favor Reaction (5) as the most plausible mechanism for braunite formation. Both Reaction (6) and (7) require oxygen in the sediments to form braunite. When we have observed evidence of oxidizing fluids moving through discrete veins or faults, we see Mn(IV) oxides in the Hotazel and Urucum examples, not braunite enrichments. It is also

difficult to envision the correct amount of oxygen being introduced post-depositionally into the whole of the Hotazel deposit to produce braunite throughout the entire formation. Thus we prefer Reaction (5), which seems the simplest explanation for a silicified Mn(III)-dominated mineral: begin with a Mn(III) oxide and add silica.

Our observations also constrain the timing of braunite formation. The euhedral braunite crystals in the Hotazel Formation cross-cut kutnohorite and are therefore definitively younger (Fig. 11). However, if manganese reduction converts Mn(IV)-oxides to Mn^{2+} , for Mn(III) production we either need secondary oxidation of the Mn^{2+} or some way to produce Mn(III) oxides from Mn(IV) oxides or Mn(II) carbonates to eventually crystallize into braunite. Experimental evidence has suggested that Mn(IV)-oxide reduction by the metal-reducing bacteria of the genus *Shewanella* may proceed through a Mn(III) step, which could be a Mn(III) oxide source (Lin et al., 2012). The difficulty here is to keep this Mn(III) from becoming fully reduced Mn^{2+} , but this could occur via more stable Mn(III)-ligand complexes (Madison et al., 2013) or the formation of Mn(III) oxyhydroxides, which can be temporarily stable (Hem and Lind, 1983; Murray et al., 1985). Another possibility is the synthesis of Mn(III)-oxyhydroxides like feitknechtite (β - $MnOOH$) from reaction of co-existing Mn^{2+} and Mn(IV) oxides (Elzinga, 2011). While any of these alternatives are possible, we do know that some Mn(III)-dominated phase must have existed in the Hotazel and Santa Cruz sediments that was ultimately stabilized as braunite, perhaps with diagenetic addition of silica, but after the precipitation of Mn(II)-carbonate.

The Santa Cruz Formation also contains caryopilite—the Mn(II) aluminosilicate member of the kaolinite-serpentine group. This mineral appears to have formed during burial diagenesis or metamorphism from late-stage alteration and silicification of kutnohorite into caryopilite. Cross-cutting relationships show caryopilite is secondary to the Mn-carbonate, and caryopilite is known as a metamorphic mineral (Brusnitsyn, 2006); thus we regard these Mn-silicates as the result of much later post-depositional processes.

Combining knowledge of Mn redox dynamics, reduction processes, and textural, mineralogical, and redox observations, we can construct a conceptual model of manganese precipitation, diagenesis, and stabilization in the geological record (Fig. 19). Mn(IV)-oxides constitute the principal mode by which Mn enters and is concentrated in marine sediments, but these are subsequently reduced either completely or partially by sedimentary organic matter and/or related reductants (e.g., sulfide). Reduction by organic matter is commonly mediated by anaerobic microbes and promotes the precipitation of Mn-carbonates, forming first Ca-rich phases like kutnohorite, but which often undergo carbonate diagenesis to produce rhodochrosite. During reduction of Mn(IV) oxides, Mn(III) oxides or complexes are produced, which later are crystallized in the presence of silica to the Mn(III)-dominated oxide, braunite.

Our observations display a general pattern of manganese deposits composed of either exclusively Mn(II) carbonates or a mixture of Mn(III) and Mn(II) phases, but what

determines which of these two assemblages occur? We have established that Mn(II) carbonates derive from Mn(IV) oxides through reduction by organic carbon, and the Mn(III) precursor phase to braunite forms via partial reduction of Mn(IV) oxides or by Mn(IV) oxides reacting with Mn(II). We hypothesize that the kinetics of Mn(IV) reduction is critical to determining whether Mn(III) phases form since the stabilization of Mn(III)-oxides requires the presence of Mn(IV) and Mn(II). However, Mn(III) can still be reduced by metal-reducing microbes (Kostka et al., 1995), and so ultimately the assemblage redox state must be determined by the amount of reductant. If organic carbon, or another chemical species able to reduce Mn(IV) oxides, is more abundant than manganese, then all of the oxidized manganese should be reduced to Mn(II) and react to form Mn(II) carbonates or diffuse away. If organic carbon or other reductants are limiting, then the surplus of manganese should result in more oxidized phases being preserved. Theoretically, this should mean that with very little organic carbon, there is potential for preserving original manganese oxides – and while this may have happened in rare instances of the Hotazel formation, it is clear that usually manganese is reduced by available electron donors. This premise of competing manganese-electron donor dynamics allows us to infer organic carbon availability in ancient paleoenvironments – such as, in the Molango shallow sea there was highly abundant organic carbon, but in the Urucum continental rift basin, manganese was more abundant than available organic carbon or other reductants.

Later metamorphic processes may transform the kutnohorite, rhodochrosite, and/or braunite into a variety of other minerals, such as the hydrated Mn(II) alumino silicate caryopilite found in the Santa Cruz Formation. Diagenetically stabilized Mn deposits may again be exposed to oxygen via uplift and surface weathering, and all the minerals will once again be fully oxidized to Mn(IV) oxides as in the Koegas, Urucum, and Kungarra examples. This will occur from abiotic weathering in the presence of O₂ (Morgan, 2005), but recent reports suggest that the oxidation of Mn-carbonates to Mn(IV) oxides may also be microbially mediated (Tang et al., 2013). Thus to achieve an accurate understanding of early Mn mineralization both unweathered core samples and lack of metamorphism are essential to determine how much Mn was delivered to the sediments and how it was transformed by diagenesis.

5. CONCLUSIONS

We combined light and electron microscopy, X-ray absorption spectroscopy, and X-ray imaging techniques to examine key manganese deposits through time and understand their mineralogy and petrogenesis in detail across multiple scales. While manganese oxidation produces Mn(IV)-dominated oxides comprising the major vector for the sedimentation and concentration of Mn in sedimentary rocks, ancient manganese deposits are composed only of Mn(II) and Mn(III) minerals (with rare exceptions of small preserved Mn(IV)-oxide inclusions). The geological record of (relatively) well-preserved manganese deposits is thus composed predominantly of kutnohorite (Mn_{0.5}Ca_{0.5}CO₃), rhodochrosite (MnCO₃), and braunite (Mn(III)₆Mn(II)O₈SiO₄). A dataset of the

abundances of Mn deposits throughout Earth history reveals major changes, with most deposits that only emerge after the rise of oxygen; a notable exception is found in the Paleoproterozoic-age Koegas subgroup of the Transvaal Supergroup, deposited just prior to the rise of oxygen, and potentially the age-ambiguous manganese enrichment in the Australian Kungarra formation. Constrained by texture-specific mineral analyses and sedimentological observations, we constructed a paragenetic model of manganese mineral formation beginning with deposition of Mn(IV)-dominated oxides leading to the early diagenetic production of carbonate phases such as kutnohorite, with potential for stabilization of Mn(III)-rich oxides (now marked by braunite) in sedimentary environments with relatively low fluxes of sedimentary organic matter, under deep burial the ingrowth of metamorphic mineral assemblage (recrystallization of carbonate phases and production of Mn(II)-silicates), and finally possible re-oxidation to Mn(IV)-oxides driven by post-depositional exposure to O₂-bearing fluids during near surface weathering. This framework provides logic to invert sedimentological, mineralogical, and textural observations of Mn-rich sedimentary rocks for the biogeochemical processes once operating in Earth (and Mars; (Lanza et al., 2014)) surface environments.

Acknowledgements

We are grateful for manuscript comments and analytical support from George Rossman. We thank the David and Lucile Packard Foundation and a NSF-GRFP grant to J.E.J. for support. We acknowledge the Lewis and Clark Foundation for funding field work for

J.E.J., the Agouron Institute for supporting both the Agouron South Africa Drilling Project, which provided core samples of the Koegas Subgroup and the Agouron Field Excursions, which allowed J.E.J. to sample the Kungarra Formation manganese; Victoria Orphan and Benjamin Harris for donating part of a deep-sea ferromanganese nodule, J.B. Maynard for contributing many Molango deposit samples, Joseph Kirschvink for donating a well-preserved sample of the Hotazel formation, Thiago Piacentini for samples of the Santa Cruz Formation, and Nic Beukes and Bertus Smith for assistance in the field. The Stanford Synchrotron Radiation Lightsource, SLAC National Accelerator Laboratory, is supported by the U.S. Department of Energy, Office of Science, Office of Basic Energy Sciences under Contract No. DE-AC02-76SF00515. SEM, EBSD, and EPMA analyses were carried out at the Caltech GPS Division Analytical Facility, which is supported, in part, by NSF Grants EAR-0318518 and DMR-0080065.

FIGURES AND TABLES

Deposit Name	Location	Age	Geologic Setting	Redox state	Mn minerals
ferromanganese nodule	South Pacific Gyre	effectively modern	Oligotrophic ocean floor	Mn(IV)	birnessite-like
Japan Sea core	Japan Sea	Pliocene-Miocene	organic-rich failed rift basin	Mn(II)	magnesite, siderite, manganooan calcite/kutnohorite, calcian rhodochrosite
Molango deposit	Mexico	Upper Jurassic (ca. 155 Ma)	carbonate platform shelf	Mn(II)	rhodochrosite, manganooan calcite
Santa Cruz deposit	Jacadiço Basin, Brazil	Neoproterozoic	lacustrine or marine gulf continental rift basin	Mn(II,III)	braunite, rhodochrosite, kutnohorite, caryopilite
<i>weathered</i>				<i>Mn(IV)</i>	<i>cryptomelane (or birnessite)</i>
Hotazel Formation	South Africa	ca. 2200 Ma	marine back-arc basin or proximal mid-ocean ridge	Mn(II,III)	braunite, kutnohorite, manganooan calcite
Koegas Subgroup	South Africa	ca. 2415 Ma	deltaic near-shore marine	Mn(II)	ferrous rhodochrosite, manganooan siderite, manganooan calcite
<i>weathered</i>				<i>Mn(IV)</i>	<i>cryptomelane or birnessite</i>

Table 1: A summary of results from examined Mn deposits.

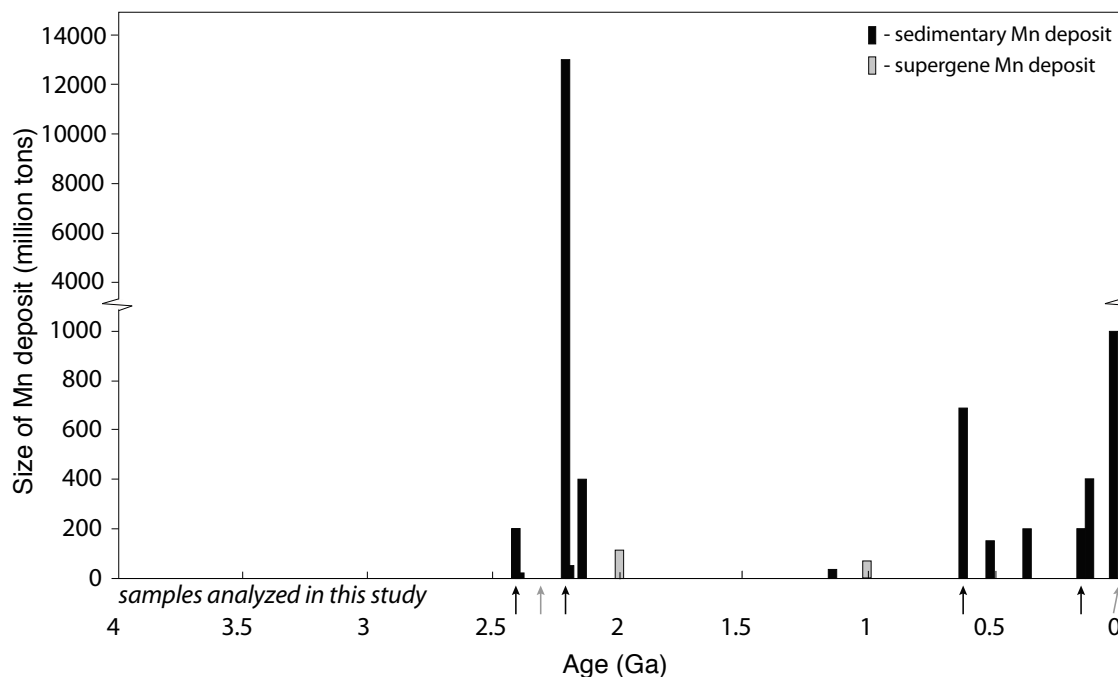
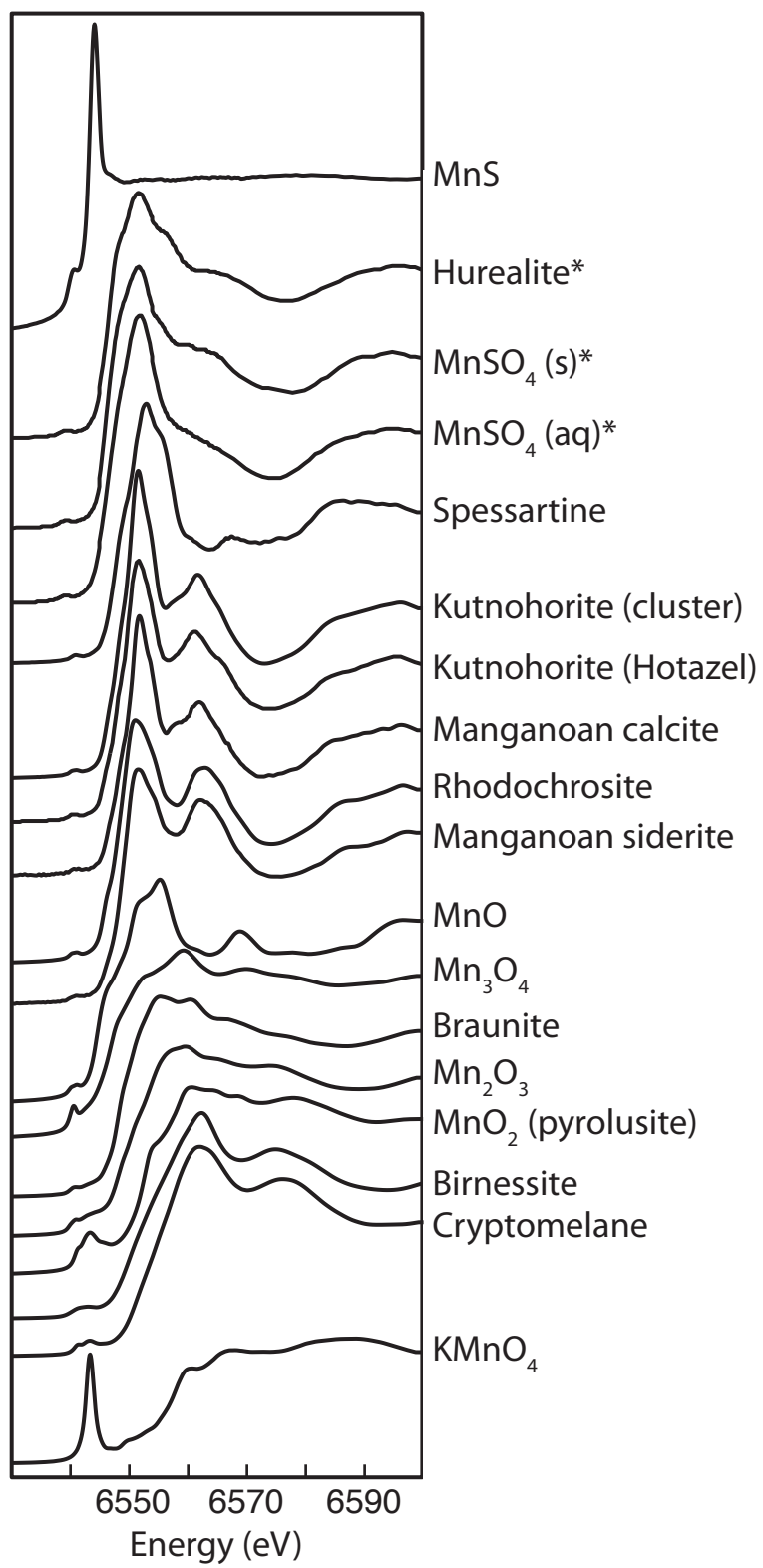


Fig. 1: Manganese ore deposits through time

Estimated volumes of major sedimentary manganese deposits plotted as a function of their best-constrained geologic age. Arrows mark deposits analyzed in this study, with black signifying large manganese deposits plotted and grey indicating timing of smaller deposits. Supergene deposits are shown in grey for cases where the age of mineralization is known; deposits from Archean proto-ore, primarily in India, occur but the age of mineralization is not known.

Fig. 2 (below): Mn K-edge X-ray absorption spectra of known manganese minerals relevant to geological deposits.

Manganese mineral standards were measured from the Caltech Mineralogical Collection, Fischer lab acquired collection. Two additional spectra for Mn(II) sulfates and a Mn(II) phosphate (marked by asterisks) are from Manceau et al (Manceau et al., 2012).



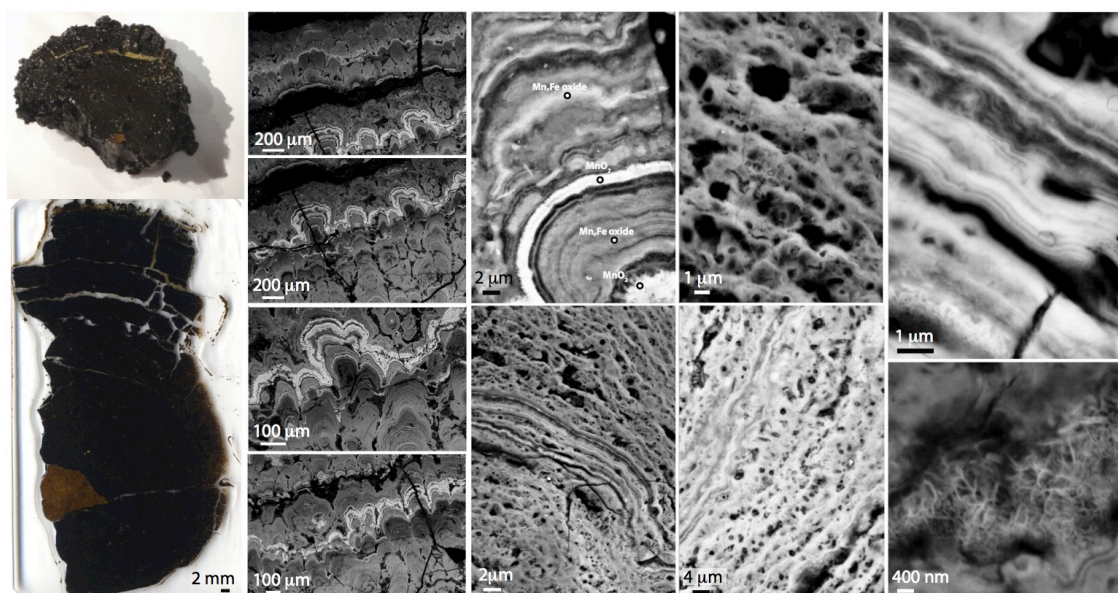


Fig. 3: Light and electron microscopy of a seafloor manganese nodule

Ferromanganese nodule from the South Pacific Gyre collected during IODP Expedition 329. Leftmost panel shows transmitted light images of the entire nodule (above) and thin section (below). Center and right panels contain electron photomicrographs of the nodule at different scales. Note the abundant isopachous and stromatolitic laminations.

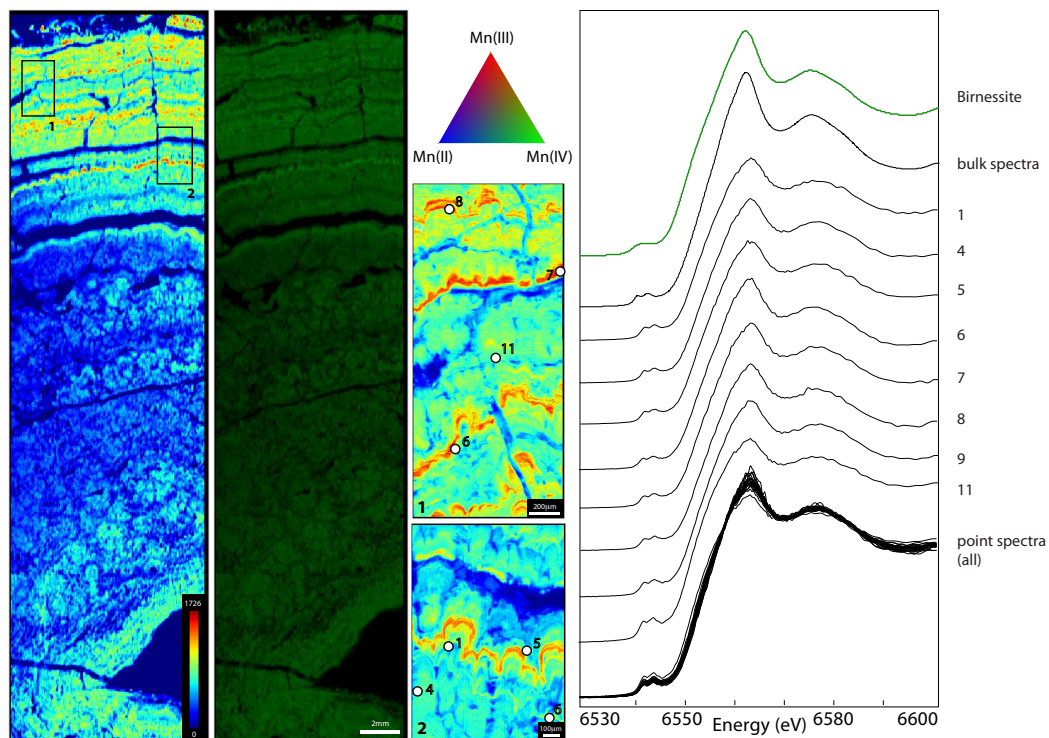


Fig. 4: Seafloor manganese nodule XAS images and spectra

X-ray absorption spectroscopy results from the modern ferromanganese nodule, showing microprobe maps of manganese concentration (jet colors in cps units), and a best-fit redox maps (tricolor RGB scale) indicating that only Mn(IV)-oxide phases are present (with Mn(II) in blue, Mn(III) in red, and Mn(IV) in green). This is supported by full XANES spectra from points throughout the nodule (marked by numbers), which indicate Mn(IV)-oxides most similar to birnessite.

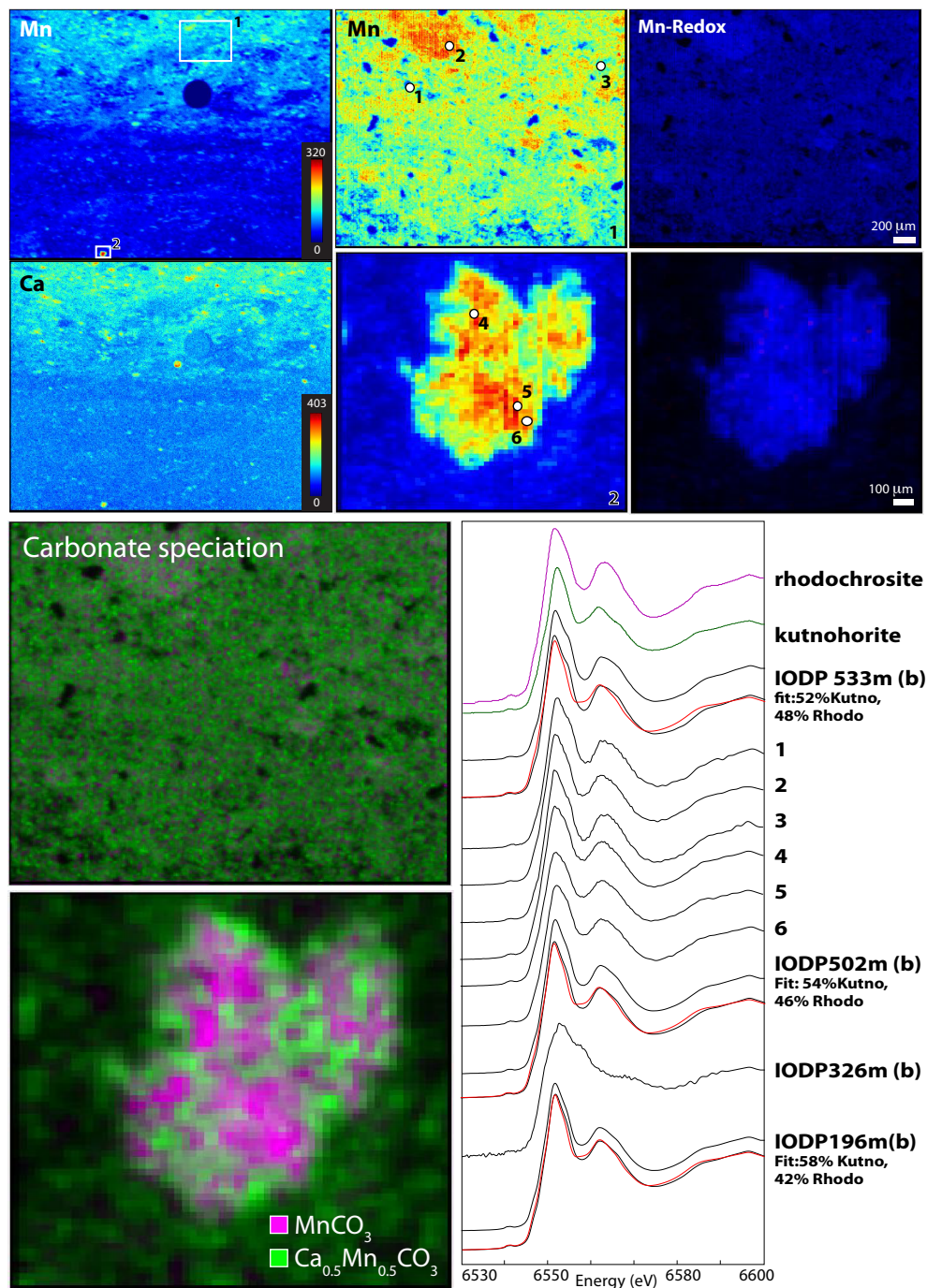


Fig. 6: Japan Sea Pliocene-Miocene sediments XAS images and spectra

X-ray absorption spectroscopy results from four samples of ODP core 799. Lithified sample at 533 m was mapped for manganese concentration (jet colors in cps units), manganese redox state (with Mn(II) in blue, Mn(III) in red, and Mn(IV) in green). The sample is comprised solely of Mn(II)-carbonate minerals; sample point spectra are plotted below standard spectra of rhodochrosite and kutnohorite. Bulk spectra were fit to

standards, with fit (red) plotted on top of and below the measured spectra (black). Best-fit estimates of rhodochrosite and kutnorhorite spectral contributions marked adjacent.

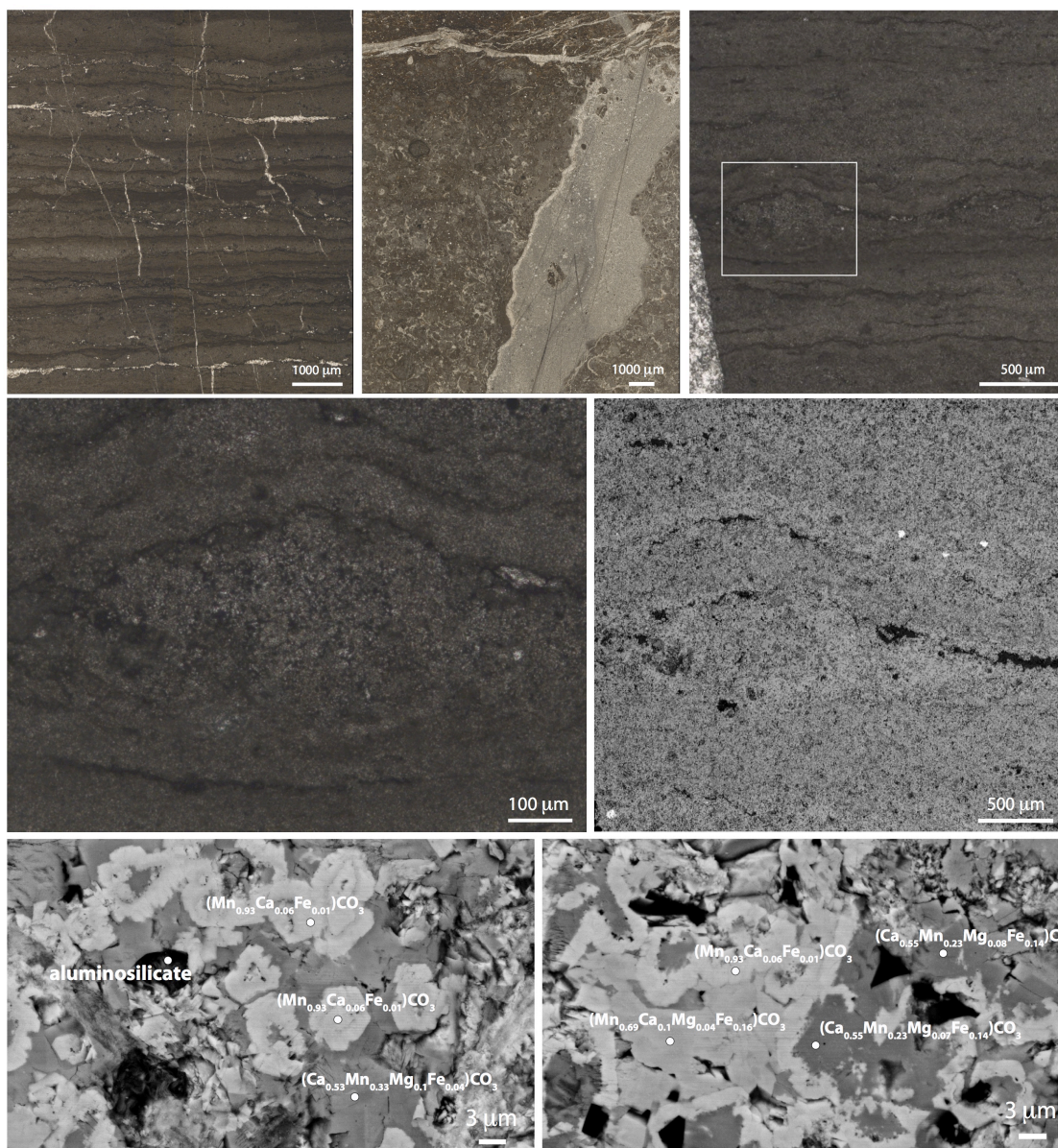


Fig. 7: Jurassic-age Molango deposit light and electron microscopy

Transmitted light (top and left) and scanning electron microscope (bottom right) images of manganese-enriched samples from the Molango deposit in Mexico. Compositional data from energy dispersive X-ray spectroscopy are summarized in text labels. The samples appear highly recrystallized and manganese is only present in carbonate minerals.

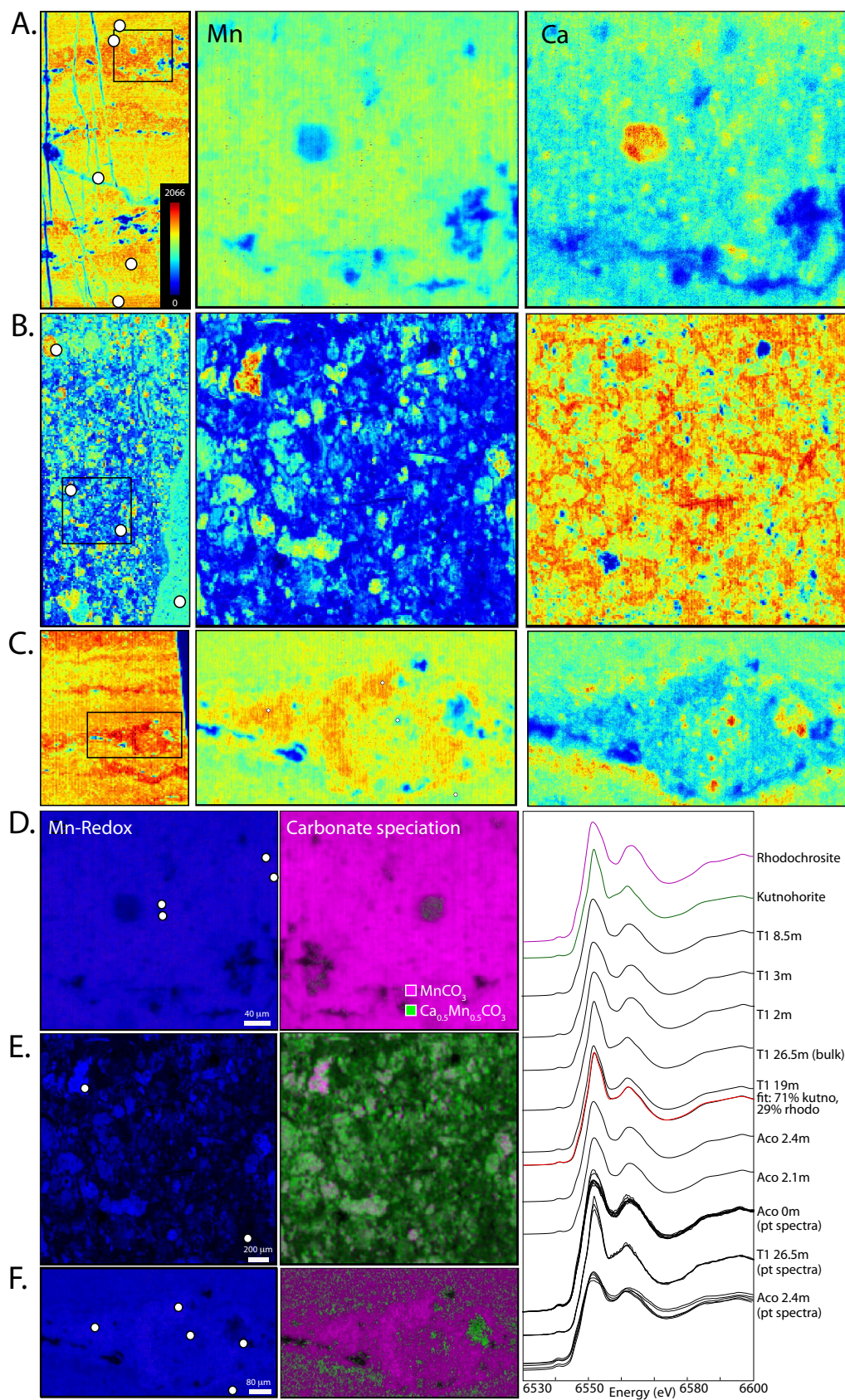
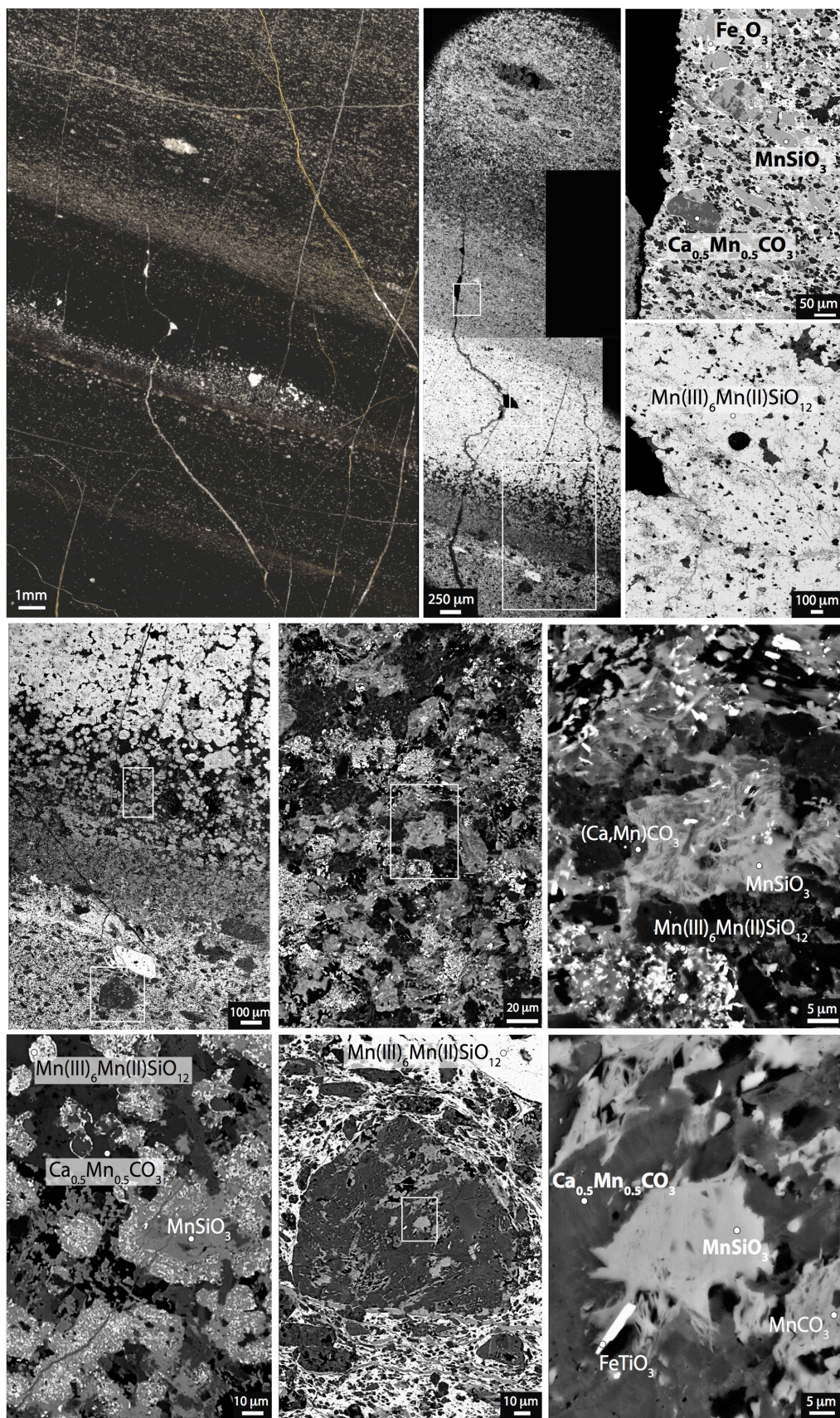


Fig. 8: Jurassic-age Molango deposit XAS images and spectra

Mn and Ca concentration (jet colors in cps units) of three samples from the Molango deposit are shown in A-C; Redox maps (Mn(II) in blue, Mn(III) in red, and Mn(IV) in green) shown below: A,D. Acoxcatlan section at 0 m. B,E. Tetzintla1 section at 26.5 m C,F. Acoxcatlan section at 2.4 m. Manganese is only present as Mn(II) in rhodochrosite and kutnohorite, as confirmed by sample spectra plotted below standard spectra of these two manganese-bearing carbonates.

Fig. 9 (below): Santa Cruz Formation light and electron microscopy

Transmitted light (left) and scanning electron microscope (right) images of manganese-rich samples from the Neoproterozoic Santa Cruz Formation from Brazil. Compositional results from energy dispersive X-ray spectroscopy spot measurements are summarized in the text labels. The sample shows a complex mineralogy and petrographic textures at a microscale. Note the presence of Mn-silicates that appear to be replacing a manganese-calcium carbonate phase.



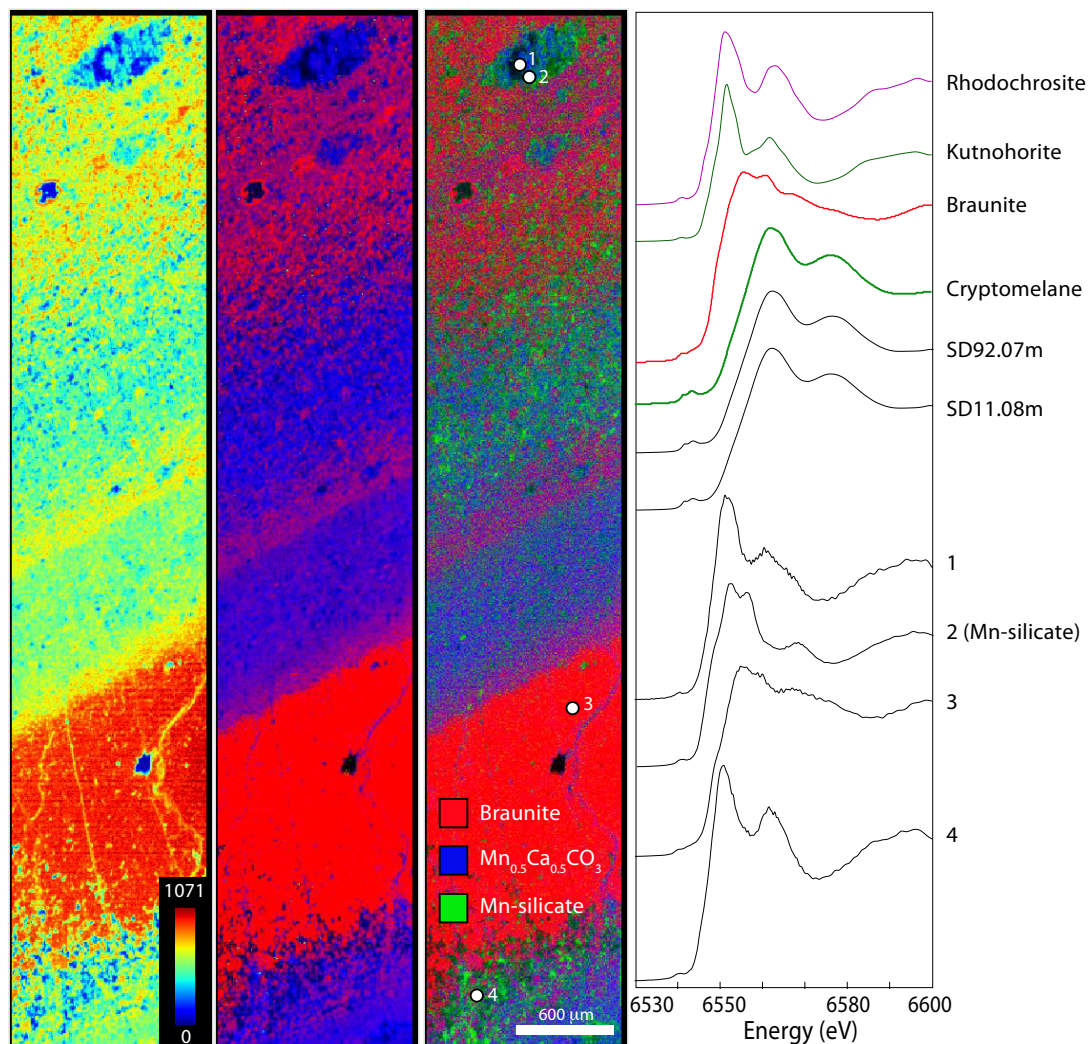


Fig. 10: Santa Cruz Formation XAS images and spectra

X-ray absorption spectroscopy results from three samples (two bulk powders, one thin section) of the Santa Cruz manganese formation. Samples were mapped for manganese concentration (jet colors in cps units), manganese redox state (tricolor RGB color scale with Mn(II) in blue, Mn(III) in red, and Mn(IV) in green), and manganese phase (with braunite in red, $\text{Mn}_{0.5}\text{Ca}_{0.5}\text{CO}_3$ in blue, and Mn-silicate identified by Raman (Fig. A2) as caryopilite in green). Measured point spectra are plotted below standard spectra and confirm the presence of rhodochrosite, kutnohorite, braunite, and cryptomelane.

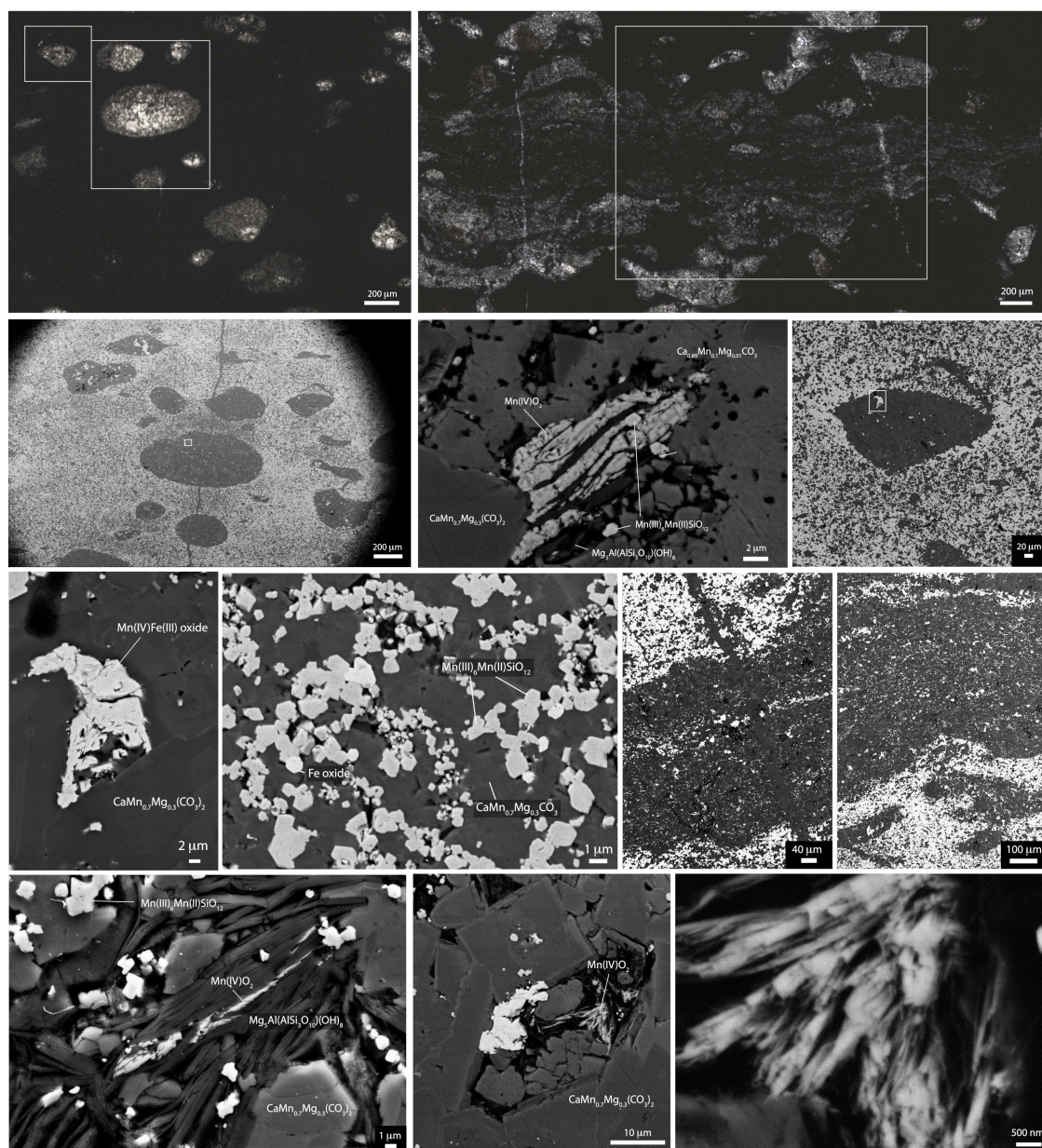


Fig. 11: Hotazel Formation light and electron microscopy

Transmitted light (top) and scanning electron microscope (bottom) images of samples from the Hotazel Formation of the Paleoproterozoic Kalahari Manganese Field from South Africa. Compositional information from energy dispersive X-ray spectroscopy spot measurements are provided in the text labels overlaid on the photomicrographs. Note the common early diagenetic Mn-carbonate nodules (light colors in transmitted light, dark in SEM backscatter contrast), floating in a dark (or backscatter-bright) Mn-oxide matrix.

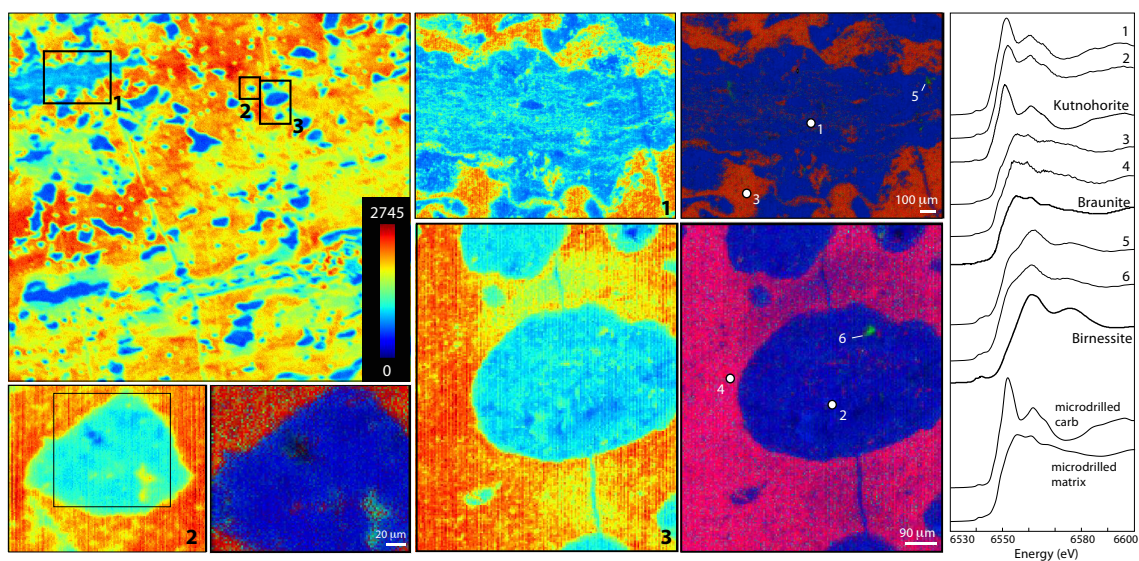


Fig. 12: Hotazel Formation XAS mapping and spectra

X-ray absorption spectroscopy of three regions of interest from Hotazel Formation samples. Samples were mapped for manganese concentration (jet colors in cps units) and manganese redox state (tricolor RGB scale with Mn(II) in blue, Mn(III) in red, and Mn(IV) in green). Phases containing Mn in all three redox states were observed in this unit. Sample spectra best matched standard spectra of kutnohorite, braunite, and birnessite (plotted above sample spectra). Note the presence of rare small inclusions of Mn(IV)-oxides preserved within nodules of kutnohorite.

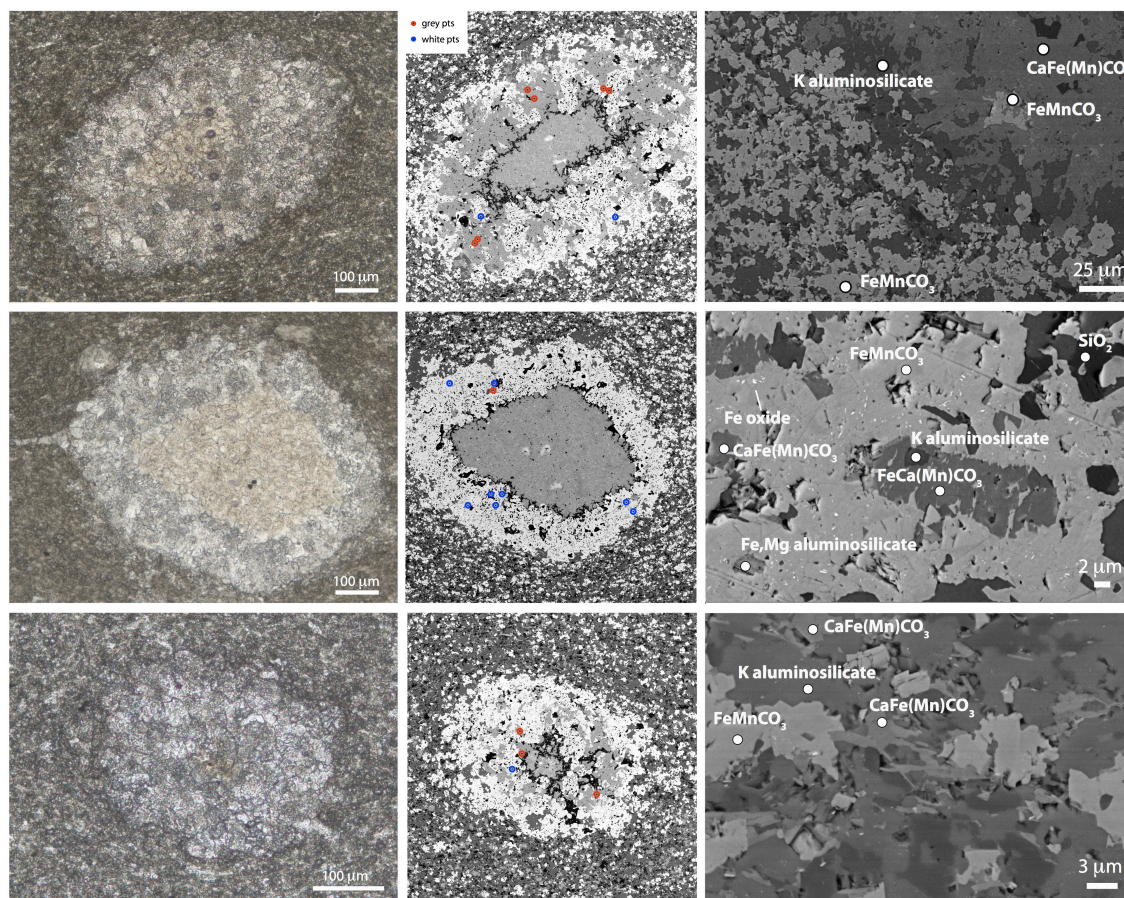


Fig. 13: Paleoproterozoic-age Koegas Subgroup light and electron microscopy
 Transmitted light (left) and scanning electron microscope (right) photomicrographs of a manganese-rich sample from the ~2.415 Ga Koegas Subgroup in South Africa. Compositional data obtained from energy dispersive X-ray spectroscopy spot measurements are summarized with text labels. Phases studied by electron microprobe wavelength-dispersive spectroscopy are indicated in red (grey/low backscatter, kutnohorite endmember) and blue (white/high backscatter, ferrous rhodochrosite endmember).

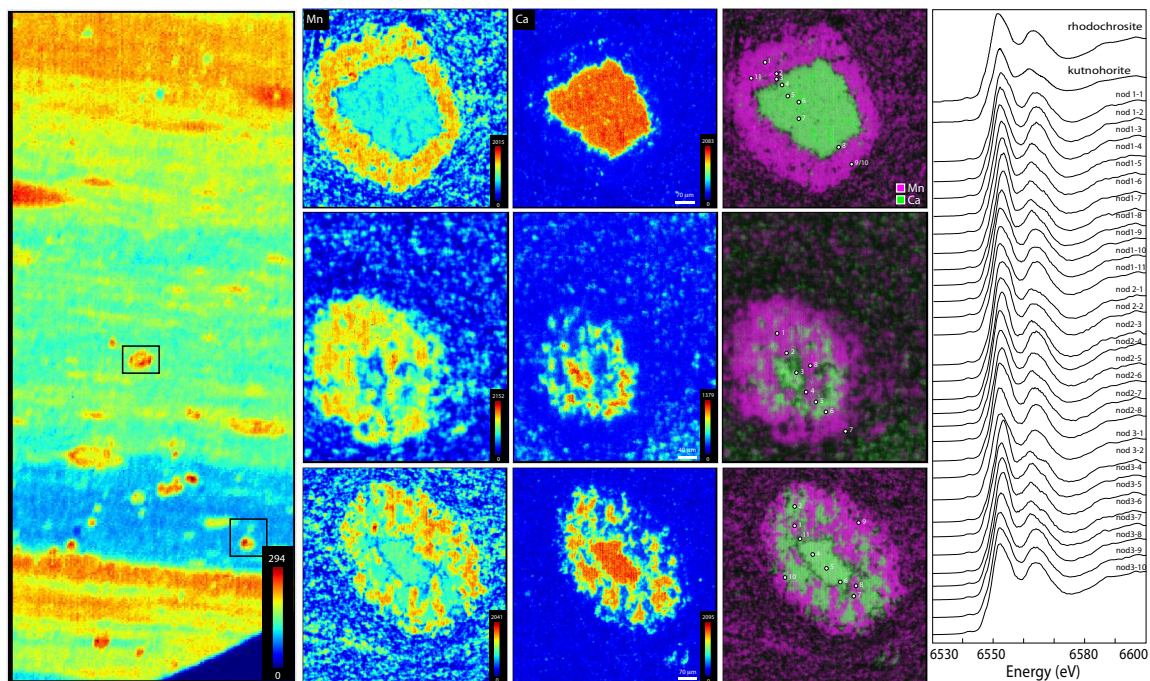


Fig. 14: Paleoproterozoic-age Koegas Subgroup XAS imaging and spectra

X-ray absorption spectroscopy results from three samples of the Koegas Subgroup. Manganese concentration (jet color scale in cps units), manganese redox state (with Mn(II) in blue, Mn(III) in red, and Mn(IV) in green), and carbonate speciation (with MnCO_3 in purple and $\text{Mn}_{0.5}\text{Ca}_{0.5}\text{CO}_3$ in green) are displayed. Numbered spots mark the locations of sample spectra, which are consistent with speciation maps and resemble standard spectra of rhodochrosite and kutnohorite.

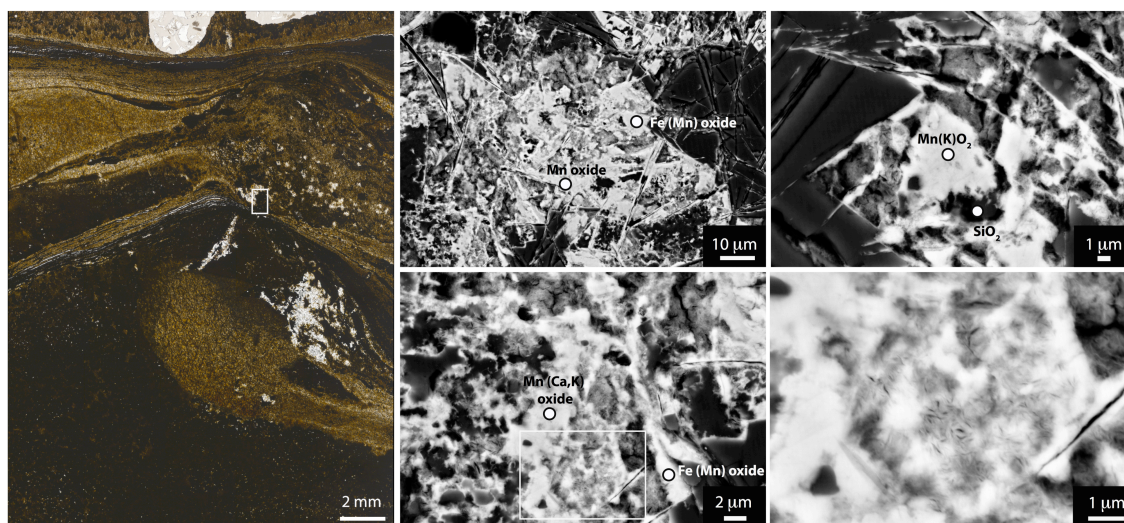


Fig. 15: Light and electron microscopy of weathered Koegas Subgroup in outcrop
 Transmitted light (left) and backscatter electron (right) photomicrographs of a microbially-bound grainstone from the Koegas Subgroup exposed at the surface in weathered outcrops in South Africa. Compositional constraints from energy dispersive X-ray spectroscopy measurements are summarized in text labels. In contrast to subsurface samples from drill cores (Figs. 13 and 14), manganese minerals appear to be predominantly oxides and manifest as fine-grained masses that mask petrographic textures.

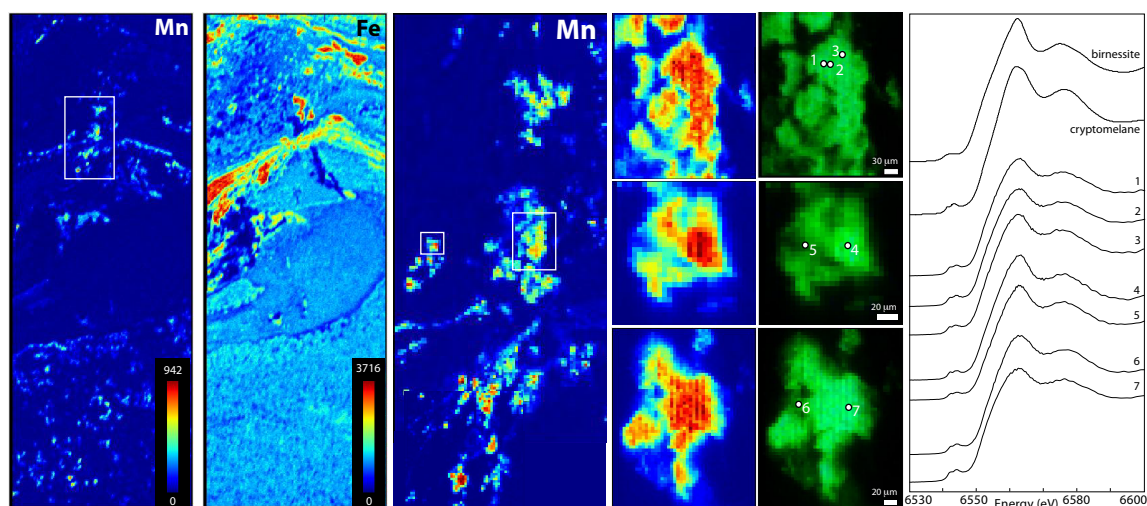


Fig. 16: XAS imaging and spectra of weathered Koegas Subgroup in outcrop
 Results of X-ray absorption spectroscopy from three regions of interest of sample of the Koegas Subgroup. Manganese concentration (in jet colors for cps units) and manganese redox state (tricolor RGB scale with Mn(II) in blue, Mn(III) in red, and Mn(IV) in green). Supporting the electron microscopy all pixels fit to Mn(IV) phases. Sample point spectra are marked and plotted to the right adjacent to their closest standard matches, cryptomelane and birnessite.

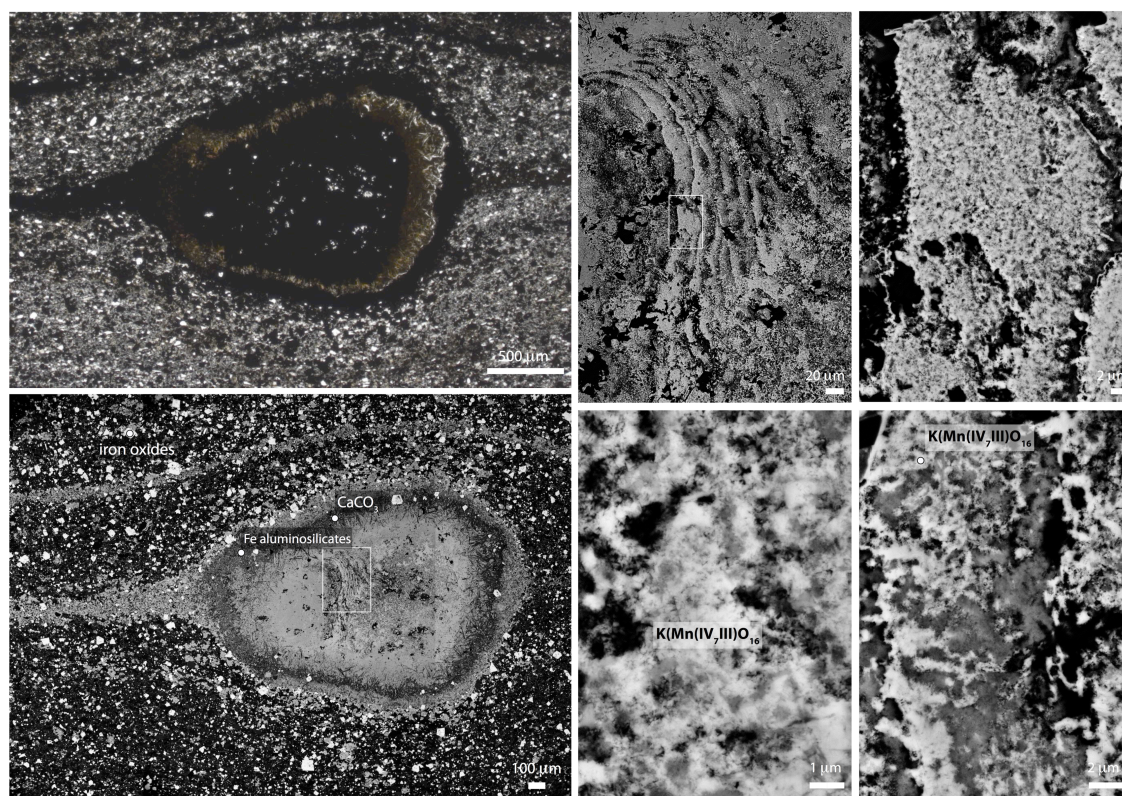


Fig. 17: Paleoproterozoic-age Kungarra Formation light and electron microscopy
 Optical (upper left) and scanning electron microscope photos of the Kungarra Formation from weathered outcrops in Australia. Compositional data from energy dispersive X-ray spectroscopy measurements are summarized in text labels. Manganese appears to be predominantly in oxide minerals of unknown redox state. Fine-scale textures are largely obliterated by growth of oxide phases, but at larger scales some nodular textures can still be observed. Note differential compaction of laminae of the nodule.

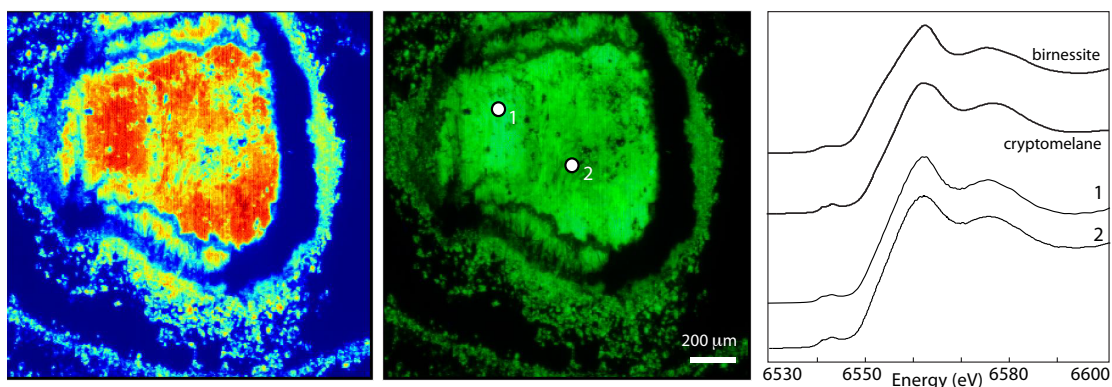


Fig. 18: Paleoproterozoic-age Kungarra Formation XAS imaging and spectra

X-ray absorption spectroscopy of three regions of interest from a weathered outcrop sample of the Kungarra Formation exposed in NW Australia. Regions were imaged for manganese concentration (jet colors in cps units) and manganese redox state (tricolor RGB image with Mn(II) in blue, Mn(III) in red, and Mn(IV) in green). The entire sample is composed of Mn(IV)-oxides. Point spectra are plotted alongside cryptomelane and birnessite.

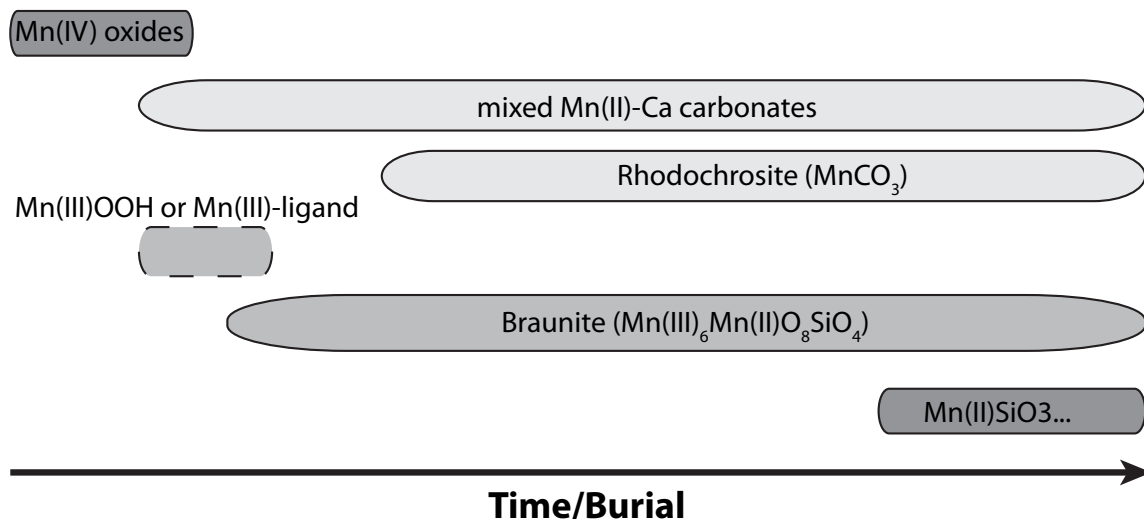


Fig. 19: Paragenetic model for the diagenetic stabilization of Mn deposits

Manganese is deposited and concentrated in sediments as Mn(IV) oxides, and subsequently reduced during organic diagenesis either partially to Mn(III) phases or fully to Mn^{2+} . Mn^{2+} is then precipitated as Mn-bearing carbonates. The most primary of these appears to be manganese-calcium carbonates like kutnohorite ($\text{Mn}_{0.5}\text{Ca}_{0.5}\text{CO}_3$) but which can with burial diagenesis yield undergo recrystallization and yield more manganese-enriched carbonate phases like rhodochrosite (MnCO_3). Mn(III)-oxide phases are silicified and stabilized as braunite ($\text{Mn(III)}_6\text{Mn(II)SiO}_{12}$). Increasing burial diagenesis and metamorphism can greatly increase the mineralogical diversity of Mn deposits, particularly with Mn-silicate minerals, including caryopilite. See text for details.

REFERENCES

- Akintola A. I., Ikhane P. R., Akintola G. ., Sanni O. G. and Oduneye O. A. (2012) Petrochemical Evaluations of the Pan African Pegmatites of Apomu Area, Southwestern Nigeria. *Environ. Nat. Resour. Res.* **2**, 8–17.
- Aller R. C. (1990) Bioturbation and Manganese Cycling in Hemipelagic Sediments. *Philos. Trans. R. Soc. Lond. Ser. Math. Phys. Sci.* **331**, 51–68.
- Aller R. C. and Rude P. D. (1988) Complete oxidation of solid phase sulfides by manganese and bacteria in anoxic marine sediments. *Geochim. Cosmochim. Acta* **52**, 751–765.
- Anbar A. D. and Holland H. D. (1992) The photochemistry of manganese and the origin of banded iron formations. *Geochim. Cosmochim. Acta* **56**, 2595–2603.
- Anderson C. R., Johnson H. A., Caputo N., Davis R. E., Torpey J. W. and Tebo B. M. (2009) Mn(II) oxidation is catalyzed by heme peroxidases in “*Aurantimonas manganoxydans*” strain SI85-9A1 and *Erythrobacter* sp. strain SD-21. *Appl. Environ. Microbiol.* **75**, 4130–4138.
- Armstrong F. A. (2008) Why Did Nature Choose Manganese to Make Oxygen? *Philos. Trans. R. Soc. B Biol. Sci.* **363**, 1263–1270.
- Bargar J. R., Tebo B. M., Bergmann U., Webb S. M., Glatzel P., Chiu V. Q. and Villalobos M. (2005) Biotic and abiotic products of Mn(II) oxidation by spores of the marine *Bacillus* sp. strain SG-1. *Am. Mineral.* **90**, 143–154.
- Bargar J. R., Tebo B. M. and Villinski J. E. (2000) In situ characterization of Mn(II) oxidation by spores of the marine *Bacillus* sp. strain SG-1. *Geochim. Cosmochim. Acta* **64**, 2775–2778.
- Bargar J. R., Webb S. M. and Synchrotron S. (2005) Structural Determination of Marine Bacteriogenic Manganese Oxides. *Sci. York*, 1–4.
- Barley M. E., Pickard A. L. and Sylvester P. J. (1997) Emplacement of a large igneous province as a possible cause of banded iron formation 2.45 billion years ago. *Nature* **385**, 55–58.
- Bekker A., Holland H. D., Wang P.-L., Rumble D., Stein H. J., Hannah J. L., Coetzee L. L. and Beukes N. J. (2004) Dating the rise of atmospheric oxygen. *Nature* **427**, 117–120.
- Bergmann K. D., Grotzinger J. P. and Fischer W. W. (2013) Biological Influences on Seafloor Carbonate Precipitation. *PALAIOS* **28**, 99–115.

- Berner E. K. and Berner R. A. (2012) *Global Environment: Water, Air, and Geochemical Cycles.*, Princeton University Press.
- Beukes N. J. (1987) Facies relations, depositional environments and diagenesis in a major early Proterozoic stromatolitic carbonate platform to basinal sequence, Campbellrand Subgroup, Transvaal Supergroup, Southern Africa. *Sediment. Geol.* **54**, 1–46.
- Beukes N. J. (1983) Palaeoenvironmental Setting of Iron-Formations in the Depositional Basin of the Transvaal Supergroup, South Africa. In *Developments in Precambrian Geology* (eds. A. F. Trendall and R. C. Morris). Elsevier, Amsterdam, The Netherlands. pp. 131–198. Available at: <http://www.sciencedirect.com/science/article/pii/S0166263508700434> [Accessed March 22, 2013].
- Brand U. and Veizer J. (1980) Chemical diagenesis of a multicomponent carbonate system; 1, Trace elements. *J. Sediment. Res.* **50**, 1219–1236.
- Brusnitsyn A. I. (2006) Mineralogy and metamorphism conditions of manganese ore at the South Faizulino deposit, the southern Urals, Russia. *Geol. Ore Depos.* **48**, 193–214.
- Büchel C., Barber J., Ananyev G., Eshaghi S., Watt R. and Dismukes C. (1999) Photoassembly of the Manganese Cluster and Oxygen Evolution from Monomeric and Dimeric CP47 Reaction Center Photosystem II Complexes. *Proc. Natl. Acad. Sci.* **96**, 14288–14293.
- Burdige D. J. and Nealson K. H. (1986) Chemical and microbiological studies of sulfide-mediated manganese reduction. *Geomicrobiol. J.* **4**, 361–387.
- Butterfield C. N., Soldatova A. V., Lee S.-W., Spiro T. G. and Tebo B. M. (2013) Mn(II,III) oxidation and MnO₂ mineralization by an expressed bacterial multicopper oxidase. *Proc. Natl. Acad. Sci. U. S. A.* **110**, 11731–11735.
- Cairncross B. and Beukes N. J. (2013) *The Kalahari Manganese Field, the adventure continues...*, Struik Nature, Cape Town.
- Calvert S. E. and Pedersen T. F. (1996) Sedimentary geochemistry of manganese; implications for the environment of formation of manganese black shales. *Econ. Geol.* **91**, 36–47.
- Calvert S. E. and Price N. B. (1970) Composition of manganese nodules and manganese carbonates from Loch Fyne, Scotland. *Contrib. Mineral. Petrol.* **29**, 215–233.

- Canfield D. E., Thamdrup B. and Hansen J. W. (1993) The anaerobic degradation of organic matter in Danish coastal sediments: Iron reduction, manganese reduction, and sulfate reduction. *Geochim. Cosmochim. Acta* **57**, 3867–3883.
- Van Cappellen P., Viollier E., Roychoudhury A., Clark L., Ingali E., Lowe K. and Dichistrina T. (1998) Cycling of iron and manganese in surface sediments; a general theory for the coupled transport and reaction of carbon, oxygen, nitrogen, sulfur, iron, and manganese. *Environ. Sci. Technol.* **32**, 2931–2939.
- Clement B. G., Luther III G. W. and Tebo B. M. (2009) Rapid, oxygen-dependent microbial Mn(II) oxidation kinetics at sub-micromolar oxygen concentrations in the Black Sea suboxic zone. *Geochim. Cosmochim. Acta* **73**, 1878–1889.
- Coleman M. L., Fleet A. and Donson P. (1982) *Preliminary studies of manganese-rich carbonate nodules from Leg 68, Site 503, eastern equatorial Pacific.*
- Cornell D. H. and Schütte S. S. (1995) A volcanic-exhalative origin for the world's largest (Kalahari) Manganese field. *Miner. Deposita* **30**, 146–151.
- Von Damm K. L. (1990) Seafloor Hydrothermal Activity: Black Smoker Chemistry and Chimneys. *Annu. Rev. Earth Planet. Sci.* **18**, 173.
- Davies S. H. R. and Morgan J. J. (1989) Manganese(II) oxidation kinetics on metal oxide surfaces. *J. Colloid Interface Sci.* **129**, 63–77.
- Dick G. J., Clement B. G., Webb S. M., Fodrie F. J., Bargar J. R. and Tebo B. M. (2009) Enzymatic microbial Mn(II) oxidation and Mn biooxide production in the Guaymas Basin deep-sea hydrothermal plume. *Geochim. Cosmochim. Acta* **73**, 6517–6530.
- Diem D. and Stumm W. (1984) Is dissolved Mn²⁺ being oxidized by O₂ in absence of Mn-bacteria or surface catalysts? *Geochim. Cosmochim. Acta* **48**, 1571–1573.
- Dollhopf M. E., Nealson K. H., Simon D. M. and Luther III G. W. (2000) Kinetics of Fe(III) and Mn(IV) reduction by the Black Sea strain of *Shewanella putrefaciens* using in situ solid state voltammetric Au/Hg electrodes. *Mar. Chem.* **70**, 171–180.
- Elzinga E. J. (2011) Reductive Transformation of Birnessite by Aqueous Mn(II). *Environ. Sci. Technol.* **45**, 6366–6372.
- Fischer T. B., Heaney P. J., Jang J.-H., Ross D. E., Brantley S. L., Post J. E. and Tien M. (2008) Continuous time-resolved X-ray diffraction of the biocatalyzed reduction of Mn oxide. *Am. Mineral.* **93**, 1929–1932.

- Fischer W. W. and Knoll A. H. (2009) An Iron Shuttle for Deepwater Silica in Late Archean and Early Paleoproterozoic Iron Formation. *Geol. Soc. Am. Bull.* **121**, 222–235.
- Fischer W. W., Schroeder S., Lacassie J. P., Beukes N. J., Goldberg T., Strauss H., Horstmann U. E., Schrag D. P. and Knoll A. H. (2009) Isotopic constraints on the Late Archean carbon cycle from the Transvaal Supergroup along the western margin of the Kaapvaal Craton, South Africa. *Precambrian Res.* **169**, 15–27.
- Fredrickson J. K., Romine M. F., Beliaev A. S., Auchtung J. M., Driscoll M. E., Gardner T. S., Nealon K. H., Osterman A. L., Pinchuk G., Reed J. L., Rodionov D. A., Rodrigues J. L. M., Saffarini D. A., Serres M. H., Spormann A. M., Zhulin I. B. and Tiedje J. M. (2008) Towards environmental systems biology of *Shewanella*. *Nat. Rev. Microbiol.* **6**, 592–603.
- Freitas B. T., Warren L. V., Boggiani P. C., De Almeida R. P. and Piacentini T. (2011) Tectono-sedimentary evolution of the Neoproterozoic BIF-bearing Jacadigo Group, SW-Brazil. *Sediment. Geol.* **238**, 48–70.
- Geszvain K., Butterfield C., Davis R. E., Madison A. S., Lee S., Parker D. L., Soldatova A., Spiro T. G., Luther G. W. and Tebo B. M. (2012) The molecular biogeochemistry of manganese(II) oxidation. *Biochem. Soc. Trans.* **40**, 1244–1248.
- Gross G. A. (1965) *Geology of Iron Deposits in Canada.*, Department of Mines and Technical Surveys, Geological Survey of Canada, Ottawa.
- Grotzinger J. P. and Kasting J. F. (1993) New constraints on Precambrian ocean composition. *J. Geol.* **101**, 235–243.
- Gutzmer J. (1996) Genesis and alteration of the Kalahari and Postmasburg manganese deposits, Griqualand West, South Africa. Rand Afrikaans University.
- Hammel K. E., Tardone P. J., Moen M. A. and Price L. A. (1989) Biomimetic oxidation of nonphenolic lignin models by Mn(III): new observations on the oxidizability of guaiacyl and syringyl substructures. *Arch. Biochem. Biophys.* **270**, 404–409.
- Hansel C. M., Zeiner C. A., Santelli C. M. and Webb S. M. (2012) Mn(II) oxidation by an ascomycete fungus is linked to superoxide production during asexual reproduction. *Proc. Natl. Acad. Sci.* **109**, 12621–12625.
- Hasui Y. and Almeida F. F. M. (1970) Geocronologia do Centro-Oeste brasileiro. *Bol. Soc. Bras. Geol. Sao Paulo* **19**, 5–26.
- Hem J. D. and Lind C. J. (1983) Nonequilibrium models for predicting forms of precipitated manganese oxides. *Geochim. Cosmochim. Acta* **47**, 2037–2046.

- Hoffman P. F. (2013) The Great Oxidation and a Siderian snowball Earth: MIF-S based correlation of Paleoproterozoic glacial epochs. *Chem. Geol.* **362**, 142–156.
- Hoffman P. F. and Schrag D. P. (2002) The snowball Earth hypothesis: testing the limits of global change. *Terra Nova* **14**, 129–155.
- Holland H. D. (1984) *The Chemical Evolution of the Atmosphere and Oceans.*, Princeton University Press.
- Iddings J. P. (2009) *Igneous Rocks: Composition, Texture and Classification, Description and Occurrence.*, Univeristy of Michigan Library, Ann Arbor.
- Ingle J. C. Jr., Suyehiro K., von Breymann M. T. and et al. (1990) *Proceedings of the Ocean Drilling Program, Initial Reports.*, Ocean Drilling Program, College Station, TX.
- Jakobsen R. and Postma D. (1989) Formation and solid solution behavior of Ca-rhodochrosites in marine muds of the Baltic deep. *Geochim. Cosmochim. Acta* **53**, 2639–2648.
- Johnson J. E., Gerpheide A., Lamb M. P. and Fischer W. W. (2014) O₂ constraints from Paleoproterozoic detrital pyrite and uraninite. *Geol. Soc. Am. Bull.* **126**, 813–830.
- Johnson J. E., Webb S. M., Thomas K., Ono S., Kirschvink J. L. and Fischer W. W. (2013) Manganese-oxidizing photosynthesis before the rise of cyanobacteria. *Proc. Natl. Acad. Sci.* **110**, 11238–11243.
- Jones S., McNaughton N. J. and Grguric B. (2013) Structural controls and timing of fault-hosted manganese at Woodie Woodie, East Pilbara, Western Australia. *Ore Geol. Rev.* **50**, 52–82.
- Junta J. L. and Hochella Jr. M. F. (1994) Manganese (II) oxidation at mineral surfaces: A microscopic and spectroscopic study. *Geochim. Cosmochim. Acta* **58**, 4985–4999.
- Junta-Rosso J. L. and Hochella Jr. M. F. (1996) The chemistry of hematite 001 surfaces. *Geochim. Cosmochim. Acta* **60**, 305–314.
- Kim S. S., Bargar J. R., Nealson K. H., Flood B. E., Kirschvink J. L., Raub T. D., Tebo B. M. and Villalobos M. (2011) Searching for biosignatures using electron paramagnetic resonance (EPR) analysis of manganese oxides. *Astrobiology* **11**, 775–786.
- Kirschvink J. L., Gaidos E. J., Bertani L. E., Beukes N. J., Gutzmer J., Maepa L. N. and Steinberger R. E. (2000) Paleoproterozoic snowball Earth: Extreme climatic and geochemical global change and its biological consequences. *Proc. Natl. Acad. Sci.* **97**, 1400–1405.

- Klein C. (2005) Some Precambrian Banded Iron-Formations (BIFs) from Around the World: Their Age, Geologic Setting, Mineralogy, Metamorphism, Geochemistry, and Origins. *Am. Mineral.* **90**, 1473–1499.
- Klein C. and Ladeira E. A. (2004) Geochemistry and Mineralogy of Neoproterozoic Banded Iron-Formations and Some Selected, Siliceous Manganese Formations from the Urucum District, Mato Grosso Do Sul, Brazil. *Econ. Geol.* **99**, 1233–1244.
- Komiya T., Hirata T., Kitajima K., Yamamoto S., Shibuya T., Sawaki Y., Ishikawa T., Shu D., Li Y. and Han J. (2008) Evolution of the composition of seawater through geologic time, and its influence on the evolution of life. *Gondwana Res.* **14**, 159–174.
- Kostka J. E., Luther G. W. I. and Nealon K. H. (1995) Chemical and biological reduction of Mn(III)-pyrophosphate complexes: Potential importance of dissolved Mn(III) as an environmental oxidant. *Geochim. Cosmochim. Acta* **59**, 885–894.
- Von Langen P. J., Johnson K. S., Coale K. H. and Elrod V. A. (1997) Oxidation kinetics of manganese (II) in seawater at nanomolar concentrations. *Geochim. Cosmochim. Acta* **61**, 4945–4954.
- Lanza N. L., Fischer W. W., Wiens R. C., Grotzinger J., Ollila A. M., Cousin A., Anderson R. B., Clark B. C., Gellert R., Mangold N., Maurice S., Le Mouélic S., Nachon M., Schmidt M., Berger J., Clegg S. M., Forni O., Hardgrove C., Melikechi N., Newsom H. E. and Sautter V. (2014) High manganese concentrations in rocks at Gale crater, Mars. *Geophys. Res. Lett.* **41**, 2014GL060329.
- Learman D. R., Voelker B. M., Vazquez-Rodriguez A. I. and Hansel C. M. (2011) Formation of manganese oxides by bacterially generated superoxide. *Nat. Geosci.* **4**, 95–98.
- Lee J.-H., Kennedy D. W., Dohnalkova A., Moore D. A., Nachimuthu P., Reed S. B. and Fredrickson J. K. (2011) Manganese sulfide formation via concomitant microbial manganese oxide and thiosulfate reduction. *Environ. Microbiol.* **13**, 3275–3288.
- Lin H., Szeinbaum N. H., DiChristina T. J. and Taillefert M. (2012) Microbial Mn(IV) reduction requires an initial one-electron reductive solubilization step. *Geochim. Cosmochim. Acta* **99**, 179–192.
- Lovley D. R. and Phillips E. J. P. (1988) Novel Mode of Microbial Energy Metabolism: Organic Carbon Oxidation Coupled to Dissimilatory Reduction of Iron or Manganese. *Appl. Environ. Microbiol.* **54**, 1472–1480.

- Lowenstein T. K., Timofeeff M. N., Brennan S. T., Hardie L. A. and Demicco R. V. (2001) Oscillations in Phanerozoic Seawater Chemistry: Evidence from Fluid Inclusions. *Science* **294**, 1086–1088.
- Luther G. W. I. (2010) The Role of One- and Two-Electron Transfer Reactions in Forming Thermodynamically Unstable Intermediates as Barriers in Multi-Electron Redox Reactions. *Aquat. Geochem.* **16**, 395–420.
- Madison A. S., Tebo B. M., Mucci A., Sundby B. and Luther G. W. (2013) Abundant Porewater Mn(III) Is a Major Component of the Sedimentary Redox System. *Science* **341**, 875–878.
- Manceau A., Marcus M. A. and Grangeon S. (2012) Determination of Mn valence states in mixed-valent manganates by XANES spectroscopy. *Am. Mineral.* **97**, 816–827.
- Martin D. M., Clendenin C. W., Krapez B. and McNaughton N. J. (1998) Tectonic and geochronological constraints on late Archaean and Palaeoproterozoic stratigraphic correlation within and between the Kaapvaal and Pilbara Cratons. *J. Geol. Soc. Aust.* **155**, 311–322.
- Matsumoto R. (1992) Diagenetic Dolomite, Calcite, Rhodochrosite, Magnesite, and Lansfordite from site 799, Japan Sea - Implications for depositional environments and the diagenesis of organic-rich sediments. In *Proceedings of the Ocean Drilling Program, Scientific Results* (eds. K. A. Pisciotta, J. C. Ingle Jr., M. T. von Breyman, and J. Barron). Ocean Drilling Program, College Station, TX. pp. 75–98. Available at: doi:10.2973/odp.proc.sr.127128-1.119.1992.
- Mayhew L. E., Webb S. M. and Templeton A. S. (2011) Microscale imaging and identification of Fe speciation and distribution during fluid-mineral reactions under highly reducing conditions. *Environ. Sci. Technol.* **45**, 4468–4474.
- Maynard J. B. (2010) The Chemistry of Manganese Ores through Time: A Signal of Increasing Diversity of Earth-Surface Environments. *Econ. Geol.* **105**, 535–552.
- McEvoy J. P. and Brudvig G. W. (2006) Water-Splitting Chemistry of Photosystem II. *Chem. Rev.* **106**, 4455–4483.
- McKeown D. A. and Post J. E. (2001) Characterization of manganese oxide mineralogy in rock varnish and dendrites using X-ray absorption spectroscopy. *Am. Mineral.* **86**, 701–713.
- Middelburg J. J., De Lange G. J. and van Der Weijden C. H. (1987) Manganese solubility control in marine pore waters. *Geochim. Cosmochim. Acta* **51**, 759–763.
- Moore T. E., Ellis M. and Selwood P. W. (1950) Solid Oxides and Hydroxides of Manganese. *J. Am. Chem. Soc.* **72**, 856–866.

- More C., Belle V., Asso M., Fournel A., Roger G., Guigliarelli B. and Bertrand P. (1999) EPR spectroscopy: a powerful technique for the structural and functional investigation of metalloproteins. *Biospectroscopy* **5**, S3–18.
- Morgan J. J. (2005) Kinetics of reaction between O₂ and Mn(II) species in aqueous solutions. *Geochim. Cosmochim. Acta* **69**, 35–48.
- Mucci A. (2004) The Behavior of Mixed Ca–Mn Carbonates in Water and Seawater: Controls of Manganese Concentrations in Marine Porewaters. *Aquat. Geochem.* **10**, 139–169.
- Müller S. G., Krapež B., Barley M. E. and Fletcher I. R. (2005) Giant iron-ore deposits of the Hamersley province related to the breakup of Paleoproterozoic Australia: New insights from in situ SHRIMP dating of baddeleyite from mafic intrusions. *Geology* **33**, 577–580.
- Murray J. W., Dillard J. G., Giovanoli R., Moers H. and Stumm W. (1985) Oxidation of Mn(II): Initial mineralogy, oxidation state and ageing. *Geochim. Cosmochim. Acta* **49**, 463–470.
- Myers C. R. and Nealson K. H. (1988) Bacterial manganese reduction and growth with manganese oxide as the sole electron acceptor. *Science* **240**, 1319–1321.
- Myers C. R. and Nealson K. H. (1988) Microbial reduction of manganese oxides: Interactions with iron and sulfur. *Geochim. Cosmochim. Acta* **52**, 2727–2732.
- Nicholson K. (1997) *Manganese Mineralization: Geochemistry And Mineralogy of Terrestrial And Marine Deposits.*, Geological Society.
- Norton J. J. (1970) Composition of a Pegmatite, Keystone, South Dakota. *Am. Mineral.* **55**, 981–1002.
- Okita P. M., Maynard J. B., Spiker E. C. and Force E. R. (1988) Isotopic evidence for organic matter oxidation by manganese reduction in the formation of stratiform manganese carbonate ore. *Geochim. Cosmochim. Acta* **52**, 2679–2685.
- Okita P. M. and Shanks W. C. (1992) Origin of stratiform sediment-hosted manganese carbonate ore deposits: Examples from Molango, Mexico, and TaoJiang, China. *Chem. Geol.* **99**, 139–163.
- Pedersen T. F. and Price N. B. (1982) The geochemistry of manganese carbonate in Panama Basin sediments. *Geochim. Cosmochim. Acta* **46**, 59–68.
- Perez J. and Jeffries T. W. (1992) Roles of manganese and organic acid chelators in regulating lignin degradation and biosynthesis of peroxidases by *Phanerochaete chrysosporium*. *Appl. Environ. Microbiol.* **58**, 2402–2409.

- Piacentini T., Vasconcelos P. M. and Farley K. A. (2013) $^{40}\text{Ar}/^{39}\text{Ar}$ constraints on the age and thermal history of the Urucum Neoproterozoic banded iron-formation, Brazil. *Precambrian Res.* **228**, 48–62.
- Pingitore Jr. N. E., Eastman M. P., Sandidge M., Oden K. and Freiha B. (1988) The coprecipitation of manganese(II) with calcite: an experimental study. *Mar. Chem.* **25**, 107–120.
- Post J. E. (1999) Manganese oxide minerals: Crystal structures and economic and environmental significance. *Proc. Natl. Acad. Sci.* **96**, 3447–3454.
- Rao A. M. F., Polerecky L., Ionescu D., Meysman F. J. R. and de Beer D. (2012) The influence of pore-water advection, benthic photosynthesis, and respiration on calcium carbonate dynamics in reef sands. *Limnol. Oceanogr.* **57**, 809–825.
- Robie R. A., Huebner J. S. and Hemingway B. S. (1995) Heat capacities and thermodynamic properties of braunite ($\text{Mn}_7\text{SiO}_{12}$) and rhodonite (MnSiO_3). *Am. Mineral.* **80**, 560–575.
- Roy S. (2006) Sedimentary manganese metallogenesis in response to the evolution of the Earth system. *Earth-Sci. Rev.* **77**, 273–305.
- Santelli C. M., Webb S. M., Dohnalkova A. C. and Hansel C. M. (2011) Diversity of Mn oxides produced by Mn(II)-oxidizing fungi. *Geochim. Cosmochim. Acta* **75**, 2762–2776.
- Schröder S., Bedorf D., Beukes N. J. and Gutzmer J. (2011) From BIF to red beds: Sedimentology and sequence stratigraphy of the Paleoproterozoic Koegas Subgroup (South Africa). *Sediment. Geol.* **236**, 25–44.
- Scott R. W. (1984) Mesozoic Biota and Depositional Systems of the Gulf of Mexico-Caribbean Region. In *Jurassic-Cretaceous Biochronology and Paleogeography of North America* (ed. G. E. G. Westermann). Geological Association of Canada. University of Toronto Press, St. John's, Newfoundland.
- Stilling A. (1998) Bulk composition of the Tanco Pegmatite at Bernic Lake, Manitoba, Canada. Masters, University of Manitoba.
- Stone A. T. and Morgan J. J. (1984) Reduction and dissolution of manganese(III) and manganese(IV) oxides by organics: 2. Survey of the reactivity of organics. *Environ. Sci. Technol.* **18**, 617–624.
- Takehara M., Komure M., Kiyokawa S., Horie K. and Yokohama K. (2010) Detrital zircon SHRIMP U-Pb age of the 2.3 Ga diamictites of the Meteorite Bore Member in the South Pilbara, Western Australia. In *Fifth International Archean*

Symposium Abstracts: Geological Survey of Western Australia (eds. I. M. Tyler and C. M. Knox-Robinson). Record 2010/18. pp. 223–224.

- Tamura N. and Cheniae G. (1987) Photoactivation of the water-oxidizing complex in Photosystem II membranes depleted of Mn and extrinsic proteins. I. Biochemical and kinetic characterization. *Biochim. Biophys. Acta BBA - Bioenerg.* **890**, 179–194.
- Tang Y., Zeiner C. A., Santelli C. M. and Hansel C. M. (2013) Fungal oxidative dissolution of the Mn(II)-bearing mineral rhodochrosite and the role of metabolites in manganese oxide formation. *Environ. Microbiol.* **15**, 1063–1077.
- Tebo B. M., Bargar J. R., Clement B. G., Dick G. J., Murray K. J., Parker D., Verity R. and Webb S. M. (2004) BIOGENIC MANGANESE OXIDES: Properties and Mechanisms of Formation. *Annu. Rev. Earth Planet. Sci.* **32**, 287–328.
- Tebo B. M., Johnson H. A., McCarthy J. K. and Templeton A. S. (2005) Geomicrobiology of manganese(II) oxidation. *Trends Microbiol.* **13**, 421–428.
- Thamdrup B., Finster K., Hansen J. W. and Bak F. (1993) Bacterial Disproportionation of Elemental Sulfur Coupled to Chemical Reduction of Iron or Manganese. *Appl. Environ. Microbiol.* **59**, 101–108.
- Thamdrup B., Rosselló-Mora R. and Amann R. (2000) Microbial Manganese and Sulfate Reduction in Black Sea Shelf Sediments. *Appl. Environ. Microbiol.* **66**, 2888–2897.
- Trouwborst R. E., Clement B. G., Tebo B. M., Glazer B. T. and Luther G. W. (2006) Soluble Mn(III) in Suboxic Zones. *Science* **313**, 1955–1957.
- Tsikos H., Beukes N. J., Moore J. M. and Harris C. (2003) Deposition, Diagenesis, and Secondary Enrichment of Metals in the Paleoproterozoic Hotazel Iron Formation, Kalahari Manganese Field, South Africa. *Econ. Geol.* **98**, 1449–1462.
- Turekian K. K. and Wedepohl K. H. (1961) Distribution of the Elements in Some Major Units of the Earth's Crust. *Geol. Soc. Am. Bull.* **72**, 175–192.
- Urban H., Stribny B. and Lippolt H. J. (1992) Iron and manganese deposits of the Urucum District, Mato Grosso do Sul, Brazil. *Econ. Geol.* **87**, 1375–1392.
- Vasconcelos P. M. (1999) K-Ar AND ⁴⁰Ar/³⁹Ar GEOCHRONOLOGY OF WEATHERING PROCESSES. *Annu. Rev. Earth Planet. Sci.* **27**, 183–229.
- Veizer J. (1978) Secular variations in the composition of sedimentary carbonate rocks, II. Fe, Mn, Ca, Mg, Si and minor constituents. *Precambrian Res.* **6**, 381–413.

- Wallmann K., Aloisi G., Haeckel M., Tishchenko P., Pavlova G., Greinert J., Kutterolf S. and Eisenhauer A. (2008) Silicate weathering in anoxic marine sediments. *Geochim. Cosmochim. Acta* **72**, 3067–3090.
- Wariishi H., Valli K. and Gold M. H. (1992) Manganese(II) oxidation by manganese peroxidase from the basidiomycete *Phanerochaete chrysosporium*. Kinetic mechanism and role of chelators. *J. Biol. Chem.* **267**, 23688–23695.
- Webb S. M. (2011) The MicroAnalysis Toolkit: X-ray Fluorescence Image Processing Software. *AIP Conf. Proc.* **1365**, 196–199.
- Webb S. M., Dick G. J., Bargar J. R. and Tebo B. M. (2005) Evidence for the presence of Mn(III) intermediates in the bacterial oxidation of Mn(II). *Proc. Natl. Acad. Sci. U. S. A.* **102**, 5558–5563.
- Webb S. M., Tebo B. M. and Bargar J. R. (2005) Structural characterization of biogenic Mn oxides produced in seawater by the marine bacillus sp. strain SG-1. *Am. Mineral.* **90**, 1342–1357.
- Wehrli B., Friedl G. and Manceau A. (1995) Reaction Rates and Products of Manganese Oxidation at the Sediment-Water Interface. In *Aquatic Chemistry Advances in Chemistry*. American Chemical Society. pp. 111–134. Available at: <http://dx.doi.org/10.1021/ba-1995-0244.ch005> [Accessed November 9, 2014].
- Wenzhöfer F., Adler M., Kohls O., Hensen C., Strotmann B., Boehme S. and Schulz H. D. (2001) Calcite dissolution driven by benthic mineralization in the deep-sea: in situ measurements of Ca²⁺, pH, pCO₂ and O₂. *Geochim. Cosmochim. Acta* **65**, 2677–2690.
- Williford K. H., Van Kranendonk M. J., Ushikubo T., Kozdon R. and Valley J. W. (2011) Constraining atmospheric oxygen and seawater sulfate concentrations during Paleoproterozoic glaciation: In situ sulfur three-isotope microanalysis of pyrite from the Turee Creek Group, Western Australia. *Geochim. Cosmochim. Acta* **75**, 5686–5705.
- Abs-Wurmbach I. (1980) Miscibility and compatibility of braunite, Mn²⁺+Mn^{6 3+}O₈/SiO₄, in the system Mn-Si-O at 1 atm in air. *Contrib. Mineral. Petrol.* **71**, 393–399.
- Ying S. C., Kocar B. D., Griffis S. D. and Fendorf S. (2011) Competitive Microbially and Mn Oxide Mediated Redox Processes Controlling Arsenic Speciation and Partitioning. *Environ. Sci. Technol.* **45**, 5572–5579.

SUPPLEMENTAL FIGURES AND TABLES

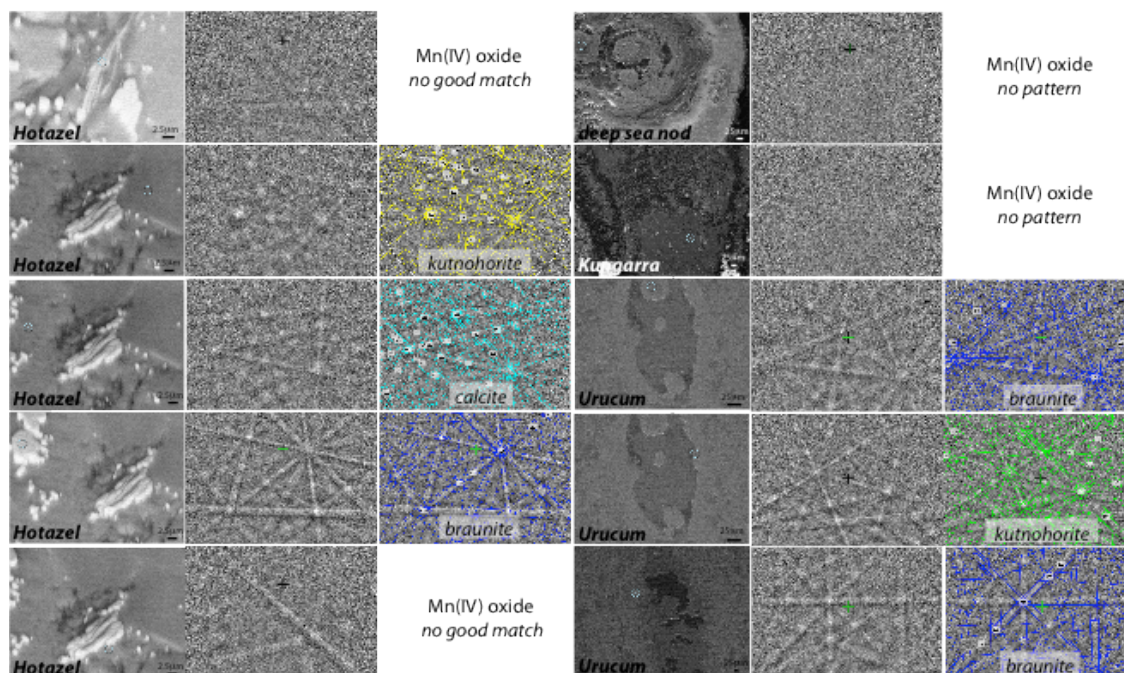
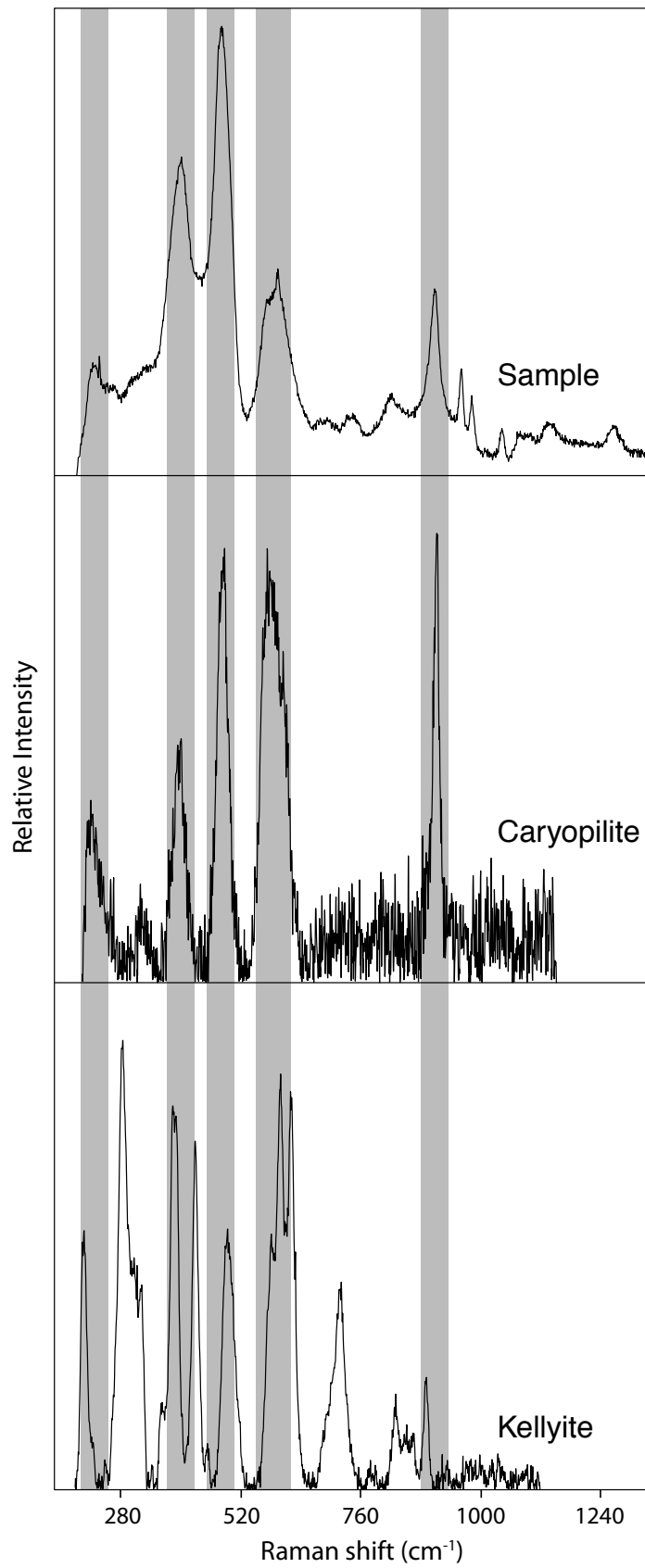


Fig. A1: EBSD patterns and identifications

Electron backscatter diffraction patterns measured on microscale phases within various samples to help assess mineralogy. These confirm phase identifications made from XANES, electron microscopy, and electron microprobe. These results also highlight that Mn(IV) oxides do not typically produce good diffraction patterns, in both ancient and modern samples.

Fig. A2 (below): Raman identification of caryopilite

Raman spectra helped constrain the identity of an unknown but common Mn-silicate observed in the Santa Cruz Formation. Two possible options from other data for this mineral were caryopilite and kellyite, but Raman shifts indicate that only caryopilite has same peaks as the sample while kellyite is a poor match for the sample.



Ore Name/Location	Volume (million tons)	Estimated Age (million years ago)	Reference
Nikopol, Ukraine, Georgia	1000	28	Varentsov and Grasselly, 1976
Groote Eylandt, Australia	400	123	Pracejus and Bolton, 1992
Molango, Mexico	200	155	Martino, 1986
Xialei, China + Atasu, Kazakhstan	200	370	Varentsov and Grasselly, 1976; Fan and Yang, 1999
Usinsk, Siberia + others	150	520	Varentsov and Grasselly, 1976
Corumbá, Brazil + small Baltic deps	686	625	Urban et al, 1992
Woodie-Woodie, Australia	65	1100-950	Jones et al, 2013
Wafangzi, China	38	1200	Rodionov et al, 2004
Sausar Group, India + Postmasburg Group	115	2000	Dasgupta et al, 1991; Gutzmer, 1996; Cairncross and Beukes, 2013
Moanda, Gabon	400	2150	National Materials Advisory Board, 1981; Gauthier-Lafaye et al, 1996
Birimian Supergroup, West Africa	49	2200	National Materials Advisory Board, 1981; Davis et al, 1994
Hotazel Formation/ Kalahari Mn field	1350	2220	Gutzmer, 1996
Minas Gerais, Brazil	20	2400	Maxwell, 1972; Babinski et al., 1995
Koegas Subgroup, S Africa	200	2420	Cairncross and Beukes, 2013

Supplementary Table 1: Survey of manganese ore deposits through geologic time, accompanying Figure 1.